Aerodynamic Shaping of a Propulsive Fuselage Concept

A Design Space Exploration

F.G.J. Topper

Technische Universiteit Delft

TU Delft

Aerodynamic Shaping of a Propulsive Fuselage Concept

A Design Space Exploration

by

F.G.J. Topper

to obtain the degree of Master of Science
at the Delft University of Technology,
to be defended publicly on Tuesday June 19, 2023 at 12:00 AM.

Student number:	4461657
Supervisor:	Dr. ir. A. Heidebrecht
Thesis Committee:	Dr. ir. R. Vos
	Dr. R. P. Dwight

TU Delft

Preface

This report marks the end of a study time in Delft. Even though I have moved to another city already, it marks the end of the life as a student. I have the warmest memories of that time. Inspired by the words of professor Wim Thijs, who taught me ”studeren is combineren”, this time brought me more than educational degrees at the TU Delft; the co-living in student houses, joining a DreamTeam, rowing intensively, creating relationships. It has all shaped me, and I could not have asked for a more beautiful place to have that. I am so grateful for all the friends, team mates, house mates and study friends that made this time as beautiful, colorful and rich as it was.

I thrive with inspiration that I take from individuals. As such, the energy of Wim Thijs attracted me towards the mechanical engineering bachelor at the TU Delft. Similarly, Roelof Vos has inspired me with his aircraft design lectures and the combination of being very knowledgeable and an incredible presenter. It is an honor having you as chair of my graduation committee. Also, I want to acknowledge the incredibly smart Peter and the most fun and enthusiastic Lennard as my sparring partners during this thesis.

A special thanks is for my thesis supervisor Alexander Heidebrecht. I could not have wished for a better supervisor. Your enthusiasm for the subject is contagious, and the time and energy you have invested in discussions with me made me feel valued. In our meetings I always felt understood and smart, but also challenged in the right proportion. If I thought I understood the matter, you managed to spark an interest to dive into the matter further. That really taught me a lot.

As a final note, I would like to thank those who are closest to me during this process. I would like to thank (all) my parents and my brother, who have always been there for me. Your advice is always spot on, and your love is unconditional, which is the pillar of myself. Lastly, I would like to thank my girlfriend Maartje. I have felt so much love, support and belief from you. Your brilliance never fails to amaze me, when you challenge me with the most relevant questions and do not let me get away with a half-hearted answer. Thank you for that.

Without the help of all the people mentioned before, I could not have finished the master’s thesis. I will, therefore, forever be grateful for them.

F.G.J. Topper
Rotterdam, May 2023

Summary

Boundary layer ingestion is an airframe-propulsion integration technology capable of enhancing aircraft propulsive efficiency. The Propulsive Fuselage Concept, a tube-and-wing layout with an rear-fuselage-mounted propulsor in the boundary layer ingestion configuration, especially takes advantage this. However, the relation between physical shape and aerodynamic performance, resulting from the complex airframe-propulsor interaction, is not entirely understood. Also, contrary to long-haul aircraft, few studies have investigated the application of the concept on medium-haul aircraft with only 10% cruise thrust contribution coming from the boundary layer ingestion propulsor, which is a top-level requirement of the *APPU* project. To facilitate parametric studies regarding these research gaps, a parametric model is developed and implemented in an engineering design application that automates aerodynamic analysis to high degree.

This thesis presents a methodology to numerically analyze axisymmetric propulsive fuselage concept designs; an engineering design application using the knowledge based engineering technology is presented that facilitates the implementation of complex engineering design rules in the construction of the parametric model. The application consist of three components.

Firstly, a flexible geometric parameterization in 2D is developed that is proven capable of constructing well-performing designs. A translation mechanism is developed between these geometric input parameters and input parameters for class shape transformation curves, which form the mathematical basis for the geometry. Secondly, the construction of a C-shaped domain and a multi-block structured mesh are also automated in the application. The mesh density for this application was verified through a mesh convergence study, and can be adjusted to fit other mesh requirements through various mesh control capabilities. Lastly, the scripted interaction between the application and ANSYS Fluent software is automated. A fan modeling methodology was developed using boundary conditions that requires only fan pressure ratio as input, while mass flow continuity through the fan is ensured. The meshing and simulation routines are validated by comparing the results of the presented routine to that of a status-quo numerical simulation. All relevant aerodynamic output parameters show agreement in a range of 3.3%.

The working of the engineering design application is demonstrated in a design space exploration based on the hypothesis that increased conicity of the rear fuselage and nacelle shape with respect to the longitudinal axis can reduce the required fan power in cruise conditions. To isolate the effect of conicity, a parameter sweep was conducted. Results show that with increasing conicity, the overall viscous dissipation was continuously reduced. Also the total pressure recovery at the fan inlet face increases up to a nacelle conical angle of 11°, after which this decays due to increased wetted area. At 11° conicity, the aerodynamic efficiency (defined as fan power required for a given net propulsive force) was increased by 0.81% relative to a less conical status-quo baseline design with 6° conicity.

The increased fuselage volume and wetted area due to increased conicity introduced the opportunity to shorten the fuselage without decreasing fuselage volume. This increased aerodynamic efficiency by 1.65% relative to the baseline. Also, as the intake diffusion functionality was redundant in this flow field, a third design was constructed with a 29% shorter intake duct, which increased aerodynamic efficiency by 1.81% compared to the baseline.

Demonstrated by these unoptimized designs and the observed physical mechanisms, it is concluded that aerodynamic efficiency could benefit from the direct and indirect effects of an increase in conicity of the propulsive fuselage concept.

Contents

Nomenclature

Greek symbols

γ	Ratio of specific heats [-]
μ	Dynamic viscosity [N s/m^2]
Φ	Viscous dissipation [W]
ϕ	Volume specific viscous dissipation [W/m^3]
ρ	Density [kg/m^3]
τ	Wall shear stress [Pa]

Roman symbols

$\dot{m}$	Mass flow rate [kg/s]
e	Mass specific energy [J/kg]
Q	Heat energy [J]
u	Mass-specific internal energy [J/kg]
W	Work [W]
y_{wall}	First wall distance [m]
A	Area [m^2]
F	Force [N]
h	Mass-specific enthalpy [m^2/s^2]
P	Power [W]
p	Pressure [Pa]
v	Velocity [m/s]

Subscripts

∞	Ambient
s	Static quantity
t	Total quantity
x	Axial direction
in	Fan intake face station
out	Fan outlet face station
$press$	Pressure
$visc$	Viscous

List of Figures

List of Tables

1 Introduction

In recent years, the aviation industry has grown at a rapid pace. This has increased global mobility and connectivity spectacularly. The industry is expected to grow even further. In 2018, EUROCONTROL published their prediction of air travel in the year 2040. The scenario they deemed most likely showed a 53% growth in annual flights in Europe [1]. Even though the global Covid-19 pandemic restricted air travel significantly, EUROCONTROL predicts a return to the amount of flights of 2019 by the year 2024 [2].

At the same time, global warming has become a more pressing issue. Sea level rise [3], ocean acidification [4] and more extreme weather events [5] have been linked to global warming, forming a direct threat to communities around the world. Aviation emissions are 2.1% of the global share, but the non-CO2 effects result in an aviation contribution to global warming of an estimated 4.9% [6].

As a result of those two developments, the environmental impact of the aviation industry is set to increase and this has sparked the public debate about this. In addition to polluting and damaging emissions, aviation uses fossil fuels for propulsion, contributing to natural resources depletion. Lastly, current transport aircraft produce noise that harms the well-being of people near airfields [7].

Various parties have expressed their vision to mitigate those effects. The European Commission presented theirs for the European aviation industry for 2050 [8]. Goals related to the mitigation of environmental impact were: a reduction of 75% CO_2, 90% NO_x and 65% noise emissions per passenger kilometer with use of available technologies and procedures, relative to capabilities of a typical new aircraft from the year 2000. In 2021, commissioned by airlines, airports and aerospace manufacturers, a road map (Figure 1.1) was presented by the Netherlands Aerospace Centre NLR to achieve ambitious environmental goals [9]. What stands out in this road map, is the large dependency on improved technology.

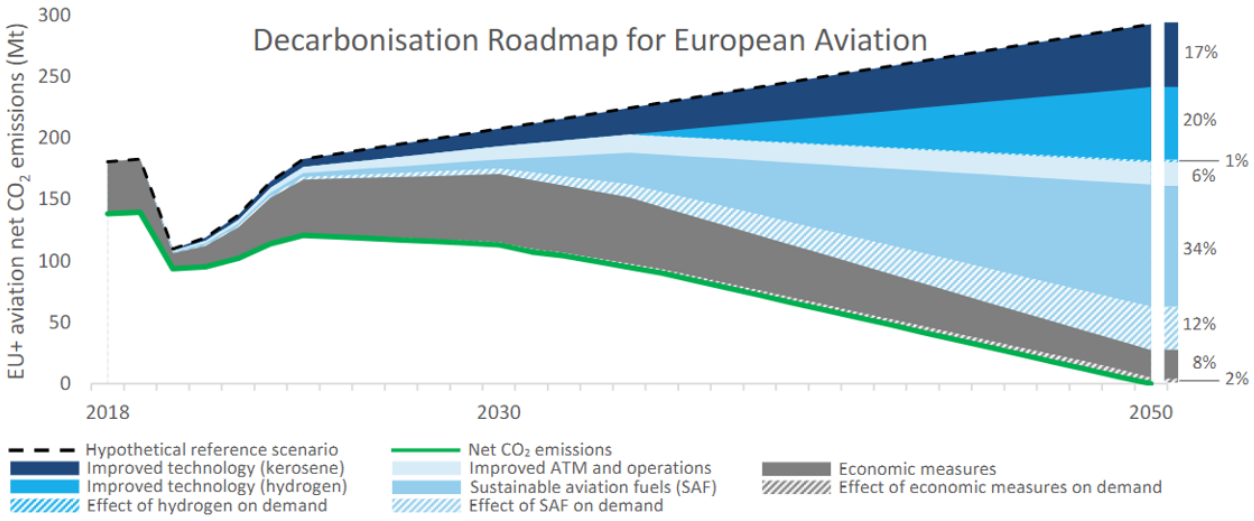

Figure 1.1: Road map to decarbonisation as envisioned by Van der Sman et al. [9]

Boundary layer ingestion (BLI) is a airframe-propulsion integration technique that has the potential to benefit from improved aero-propulsive efficiency to achieve mission fuel burn reduction between 2.8 and 3.7% [10]. The main aerodynamic benefit of BLI is the reduction of viscous dissipation of momentum [11], which means that less useful energy is lost as heat due to performed work between shearing fluid layers [12]. This is realized by placing the propulsor such that it ingests the boundary layer that is formed over the airframe body upstream of the propulsor intake. This way, the momentum surplus of the propulsor and momentum deficit behind the airframe (partially) cancel each other out, resulting in less extreme velocity gradients in the flow that cause viscous dissipation. This is called *wake-filling* and the reduction in viscous dissipation relative to a non-BLI aircraft is visualized by Uranga et al. in Figure 1.2[11].

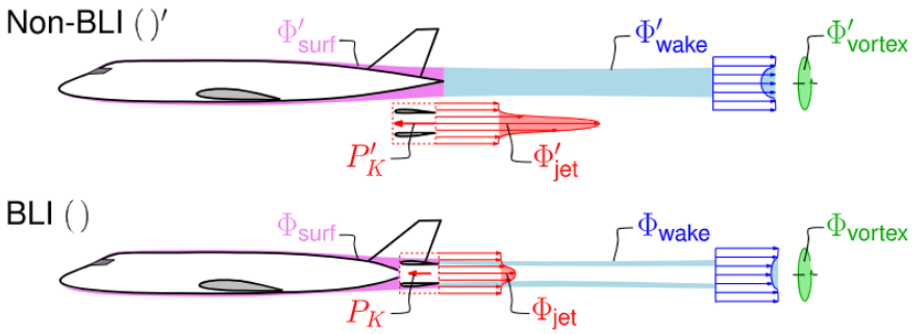

Figure 1.2: The concept of boundary layer ingestion visualized by Uranga et al.[11]. Φ indicates viscous dissipation.

Additional emerging effects such as the redundancy of pylons and smaller engines have expected aerodynamic benefits through wetted-area and weight reduction.

The *Propulsive Fuselage Concept* (PFC) is one concept exploiting BLI. This concept entails an annular intake BLI propulsor (a ducted fan in this study) on the rear-most cone of the fuselage. This has especially beneficial features. Firstly, the annular intake ingests the total circumference of the fuselage boundary layer, thereby maximizing the effect of the BLI layout [13, 14]. Secondly, little circumferential flow distortion is expected at the inlet of the propulsor relative to other BLI concepts [14]. Thirdly, this conventional base layout allows BLI to be applied on existing tube-and-wing type aircraft without a full redesign of the airframe. Lastly, by means of the closer placement of the propulsor to the longitudinal axis, the one-engine-inoperative condition is less stringent, allowing smaller yaw-surfaces. A timeline of BLI research efforts shows most recent research on BLI technology is in the context of PFC configurations, confirming high potential of this layout [15].

1.1. APPU project

The *Advanced Propulsion and Power Unit* (APPU) project is a collaborative research project by the TU Delft and industry partners aimed at significantly cutting local air emissions by applying the propulsive fuselage concept on an Airbus A321Neo. The introduced BLI propulsor is powered by the auxiliary power unit (APU), which is replaced by a system with a state of the art gas turbine fuelled by hydrogen. The hydrogen storage tank is housed in the rear of the fuselage.

1.2. Literature gap and hypothesis

Even though the PFC layout could contribute to solving the described environmental challenges, the literature review preceding the present study exposed a literature gap and pointed at a hypothesis. The literature gap is a lack of knowledge on how to shape the PFC's rear-fuselage and aerodynamic installation of the BLI propulsor (intake, cowling and exhaust). Previous studies have mainly focused on system level performance and sensitivity to operational parameters, such as the effect of *fan pressure ratio* (FPR) [16], flight level and flight Mach number [17]. Also, the effect of fuselage upsweep, wing root downwash and the empennage presence have been studied [18, 19, 20]. However, for the

shaping of the intake, exhaust and cowling of the PFC, some studies have used numerical optimizers and others used engineering intuition. As phrased by Habermann et al.: *"Some of the fundamental principles that relate the physical shape of a fuselage-propulsor to the potential benefit of boundary layer ingestion are still not fully understood."* [17].

In addition to shaping, this literature gap extends to aircraft and propulsor scales and proportions; the PFC has been extensively studied on configurations that are based on long-haul baseline aircraft that demand a thrust or propulsive power contribution from the BLI propulsor of around 30 to 33% of the aircraft's total ([14, 21]). In contrast, little research is conducted into the implementation of BLI on smaller aircraft, as recognized by Diamantidou [15]. The proposed APPU concept aims to apply the PFC concept on a short- to medium-haul Airbus A321Neo aircraft, demanding only 10% of the aircraft's total cruise thrust from the BLI propulsor. These high-level specifications imply that both the scale of the aircraft and the scale of the propulsor are smaller than previously researched. The resulting shape proportions introduce an opportunity to ingest a boundary layer portion that is closer to the wall than in previous studies, meaning that the propulsor operates in a relatively slow aerodynamic flow.

Additionally, it was recognized that studied PFC shapes feature nacelle and aft fuselage geometries that are close to parallel to the aircraft longitudinal axis. Matesanz-Garcia et al. show a design progression (Figure 1.3) yielding 2% drag decrease from DES-0 to C [22]. From this design progression the following shape developments are observed:

1. The intake duct is increasingly aligned with the incoming flow, which is has a radial component upstream of the BLI fan. As a result, the flow is turned less towards an axis-parallel direction before the fan, which could reduce total pressure loss in the flow.

2. The fuselage concavity just upstream of the fan is reduced. This visibly leads to a smaller zone of low Mach number, indicating less slowing down of the flow. This indicates a reduced adverse pressure gradient upstream of the intake. This reduces the risk of boundary layer separation.

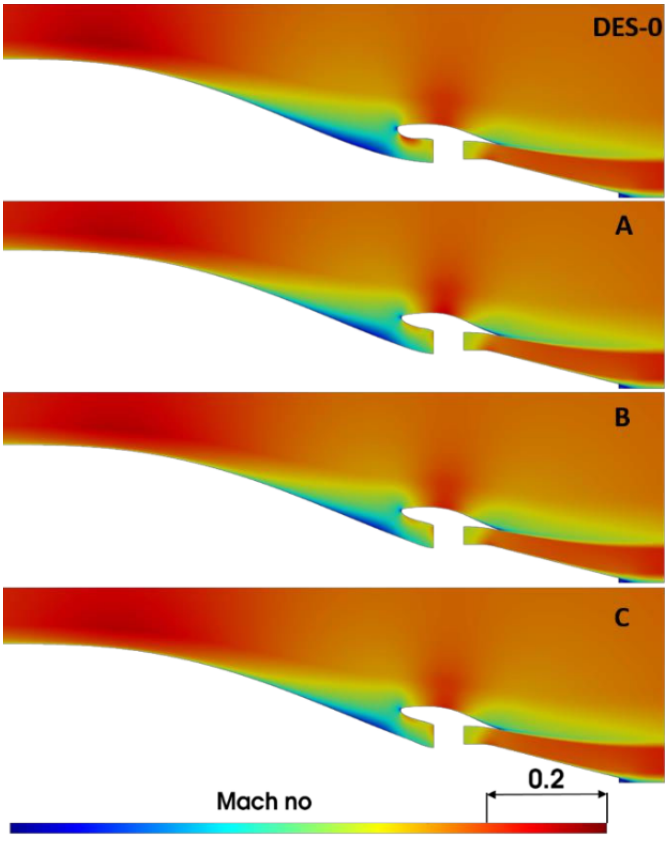

Figure 1.3: Design study by Matesanz-Garcia et al. showing an improving design progression from DES-0 to C. [22]

Based on these literature gaps and shaping ideas distilled from Matesanz-Garcia et al., it is hypothesized that the aerodynamic design of the PFC can be improved by increasing the *conicity* of the rear fuselage and nacelle. With *conicity*, the angle between the contour and the aircraft longitudinal axis is meant.

In addition to aerodynamic benefits, the increased conicity could increase the fuselage volume for a given fuselage length, thereby increasing the available volume for the APPU hydrogen tank storage. Alternatively, the fuselage could be shortened for a given fuselage volume, alleviating the ground clearance problem during rotation at the runway caused by the introduction of a ducted fan at the tail cone.

1.3. Research objectives, questions and scope

The exposed literature gap shows the relevance to have a model that facilitates geometrical design space explorations, especially in the areas of aircraft and propulsor scales and proportions, and detailed shape of the PFC. To keep the model applicable for all mentioned, but possibly even more design space explorations, the tool has to be parametric. This study firstly focuses on the parametric model and its implementation in an engineering design application. The application is then used to explore the design space of a conical PFC design in order to test the hypothesized design direction of increased conicity.

1.3.1. Research questions and objectives

Based on the literature gap, the following research questions are formulated:

1. How can the shape of the axisymmetric PFC be parameterized efficiently and flexibly to define a conical PFC geometry? And how can the PFC contour be mathematically defined with those parameters?
2. What engineering rules from off-design conditions and other engineering disciplines bound the design space to ensure feasibility of the design?
3. Is increasing the conicity of the rear fuselage and nacelle a beneficial design direction to achieving higher aerodynamic efficiency in the propulsive fuselage concept (PFC)?
   (a) How does increasing the conicity of the PFC configuration affect the aerodynamic flow field relative to an axis-parallel PFC design?
   (b) What implications does the increased conicity have on the rest of the PFC geometry? Do these implications induce opportunities to further improve aerodynamic efficiency of the design?
   (c) What physical mechanisms in the changing flow field underlie the aerodynamic efficiency?

To answer the above questions, the research objective and its sub-objectives are formulated as:

To develop an engineering design application that automates parametric model generation, meshing and CFD (RANS) simulation and to exploit it to explore the design space of conical PFC designs to identify aerodynamic mechanisms that dominate aerodynamic performance.

1. To develop an engineering design application that automates 2D parametric model generation, meshing and CFD (RANS) simulation that is capable to facilitate implementation of engineering rules.
2. To develop a CFD fan model using boundary conditions with only fan pressure ratio as input.
3. To validate the aerodynamic results of the application routine using a validation study of a status-quo PFC design.

4. To iteratively design a conical PFC configuration based on aerodynamic flow fields and other CFD results.

Note: the parameterization intended in research question 1 is defined as the set of geometric input parameters that the designer of the PFC interacts with.

1.3.2. Research scope and simplifications

The scope of this research is limited to aerodynamics, in cruise conditions specifically. The cruise conditions are taken from the APPU design cruise conditions. This entails flight at a Mach number of 0.78, at an altitude of flight level 350 (FL350 = 10668m). All atmospheric conditions are derived from this.

Furthermore, the geometry is kept to a 2D axisymmetric shape. Relative to 3D, this keeps the design space compact, simplifies the meshing procedure and reduces the computational effort. However, even though differences between 2D axisymmetric and 3D analysis may be expected, Van Sluis showed 2D axisymmetric RANS approximates 3D RANS for axisymmetric PFC designs [20].

As a supplement to the nomenclature, the following naming conventions are used in this study:

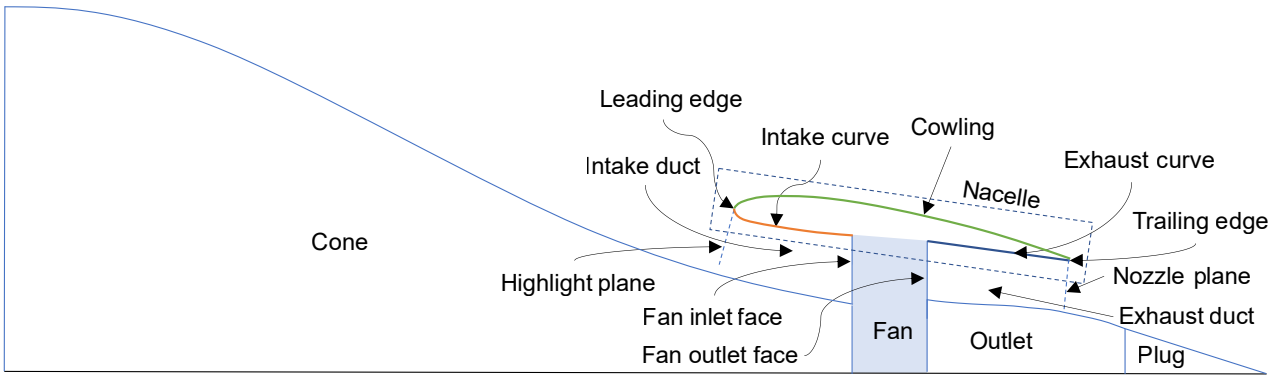

Figure 1.4: Nomenclature of different segments of the rear PFC geometry

2
Performance evaluation and metrics

The classic notions of thrust and drag, as commonly used in aircraft design, become ambiguous in tightly coupled aero-propulsive layouts such as BLI, in which thrust and drag components overlap [11, 23]. Also, the commonly used Froude-efficiency as a propulsive efficiency metric may exceed unity in BLI configurations [24]. Therefore, other metrics are used in order to assess aerodynamic performance. The main performance metric used in this study is the fan power (P_{fan}) for a given net propulsive force (NPF). Mathematical definitions of the metrics are given below.

2.1. Fan power

The power that the fan exerts on the flow is defined as the *Fan power* (P_{fan}). This metric is the measure of how much energy is put into the flow by the fan and therefore indicative of the power and fuel consumption of the aircraft. This metric is to be minimized. The expression for fan power is directly derived from the first law of thermodynamics, in the form of the energy balance over the fan, which is viewed as a control volume. This equation shows that the change in the internal energy in the control volume is equal to the heat added to the system minus the work done by the system.

$$\dot{Q} - \dot{W} = \dot{E} \tag{2.1}$$

This can be rewritten using Reynolds Theorem, in terms of mas-specific energy e. As steady flow is assumed, the time derivative is crossed out:

$$\dot{E} = \frac{d}{dt}\left[\cancel{\int_{CV} e\rho dV}\right] + \int_{CS} e\rho(\mathbf{V}\cdot\mathbf{n})dA \tag{2.2}$$

The fan is assumed to be isentropic, which means the compression is adiabatic and reversible. As the system is adiabatic, the heat flux $\dot{Q} = 0$. The work power done by the system $\dot{W}$ can be split into a pressure and shaft power component:

$$\dot{W} = \dot{W_{shaft}} + \dot{W_{pressure}} = \dot{W_{shaft}} + \int_{CS} p(\mathbf{V}\cdot\mathbf{n})dA \tag{2.3}$$

Combining Equation 2.1 and Equation 2.3:

$$-\dot{W_{shaft}} = \int_{CS}\left(e + \frac{p}{\rho}\right)\rho(\mathbf{V}\cdot\mathbf{n})dA \tag{2.4}$$

The mass-specific system energy consists of an internal energy term u and a kinetic energy term $\frac{1}{2}V^2$. Using this in Equation 2.1 and recognizing the specific total enthalpy h_t is defined as $h_t = u + \frac{p}{\rho} + \frac{1}{2}V^2$ [25], the last equation can be written as:

$$-\dot{W_{shaft}} = \int_{CS} h_t\rho(\mathbf{V}\cdot\mathbf{n})dA \tag{2.5}$$

Rewriting the right hand side of the last equation as:

$$\int_{CS} h_t\rho(\mathbf{V}\cdot\mathbf{n})dA = \sum(h_{t,out}\times\dot{m_{out}}) - \sum(h_{t,in}\times\dot{m_{in}}) \tag{2.6}$$

The fan has a single in- and outlet, which obeys the mass continuity condition ($\dot{m_{fan}} = \dot{m_{in}} = \dot{m_{out}}$). Also, the fan efficiency is assumed to be unity, implying fan power = shaft power performed on the mass flow of air. As the shaft power performed by the fan equals minus shaft power performed on the mass of air we can write:

$$-\dot{W_{shaft}} = P_{fan} = \dot{m_{fan}} \left(h_{t,\text{out}} - h_{t,\text{in}}\right) \tag{2.7}$$

2.2. Net Propulsive Force

To avoid the need to split thrust and drag components, the resultant axial force of the overall configuration is calculated and called *Net Vehicle Force* (NVF) [19]:

$$NVF = F_{fan} - F_{\text{surf}} = \dot{m_{fan}} \left(v_{x,out} - v_{x,in}\right) + A_{out} p_{s,out} - A_{in} p_{s,in} - \sum_i \iint_{S_i} \left(p_s n_x + \tau_w\right) dS_i \tag{2.8}$$

The NVF (positive direction defined in the thrust direction) is used to calculate the net axial force addition of the integration of the propulsion system, the *Net Propulsive Force* (NPF). In the present study, the NPF is the force metric of interest and it is defined as the net axial force addition relative to a baseline non-BLI fuselage. It is defined as:

$$NPF = D_{no-BLI,fus} + NVF \tag{2.9}$$

in which $D_{no-BLI,fus}$ is the drag of the non-BLI baseline fuselage.

2.3. Intake Pressure Recovery

While the two previous metrics reflect global performance, the performance of the intake is measured by means of the intake pressure recovery metric (IPR), defined as the ratio of area averaged total pressure at the highlight plane and at the fan intake face.

$$IPR = \frac{\overline{p_{t,in}}}{p_{t,highlight}} \times 100\% \tag{2.10}$$

Pressures, both total and static, will be presented as dimensionless coefficients relative to the ambient pressure. Static and total pressure coefficients are defined respectively as:

$$C_p = \frac{p - p_\infty}{\frac{1}{2}\rho_\infty V_\infty^2} \tag{2.11}$$

$$C_{p,t} = \frac{p_t - p_\infty}{\frac{1}{2}\rho_\infty V_\infty^2} \tag{2.12}$$

2.4. Viscous dissipation

As the reduction of viscous dissipation is the largest benefit of BLI, this term is useful to look at. It is plotted in contours as a field quantity and it is used as an indicator of where useful energy is converted into heat. According to Frank M. White [25], the viscous dissipation term per unit volume for an incompressible Newtonian fluid can be expressed as:

$$\phi = \mu \left[2\left(\frac{\partial u}{\partial x}\right)^2 + 2\left(\frac{\partial v}{\partial y}\right)^2 + 2\left(\frac{\partial w}{\partial z}\right)^2 + \left(\frac{\partial v}{\partial x} + \frac{\partial u}{\partial y}\right)^2 + \left(\frac{\partial w}{\partial y} + \frac{\partial v}{\partial z}\right)^2 + \left(\frac{\partial u}{\partial z} + \frac{\partial w}{\partial x}\right)^2 \right] \tag{2.13}$$

Integrated over the entire domain, referred to as control volume CV, the total loss due to viscous dissipation is calculated as:

$$\Phi = \int_{CV} \phi dV \tag{2.14}$$

3
Numerical modeling methodology

An engineering design application is developed that drastically reduces the design and analysis time of an instance of the intended PFC designs. It is developed using the *knowledge based engineering* (KBE) software *ParaPy*, which facilitates automation of large segments of the engineering work flow in design space explorations; in this application, these segments are the construction of the geometry, multi-block domain and structured mesh, and the scripted communication (*interface*) between the application and a third-party CFD software. In addition to this high level of automation, KBE allows complex engineering design rules to be used in the generation of the parametric model, which presents an opportunity to feed back learned design rules into the application regarding the design of the PFC. This means learned knowledge can be re-used by next users of the application. The workflow of the developed application is shown in the following diagram:

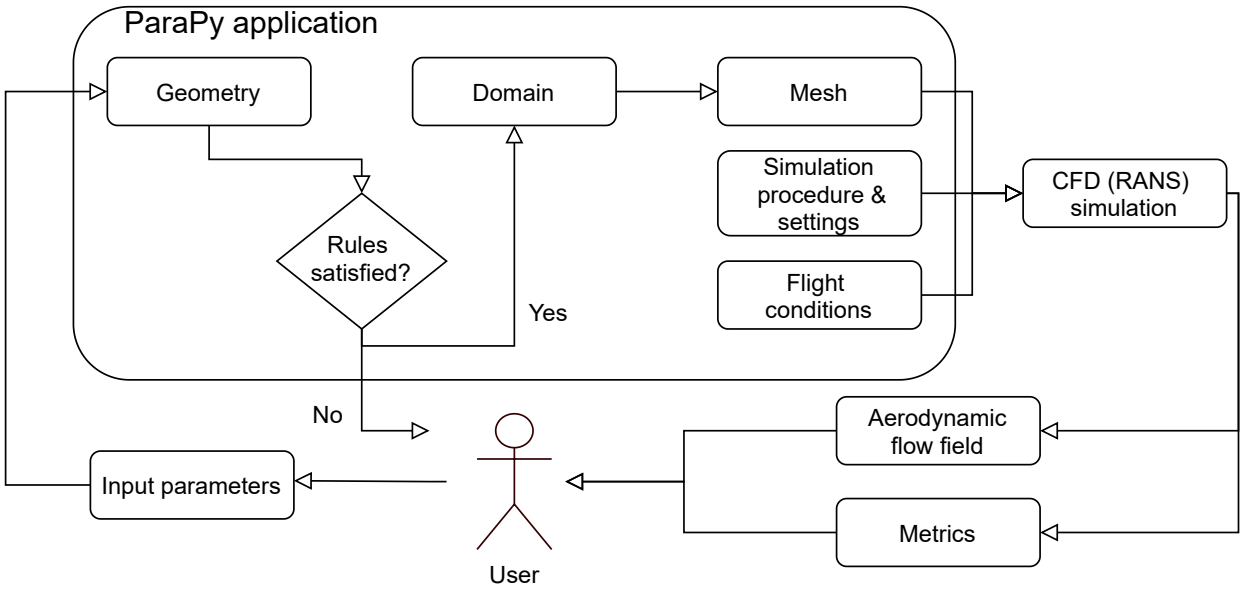

Figure 3.1: ParaPy application workflow diagram

First, the user specifies the inputs of the parametric geometry. Only if this geometry complies with the set engineering rules, the step of domain and mesh construction is available. After the simulation procedure and flight conditions are specified, the CFD simulation is invoked. Based on the CFD outputs, a new design iteration is made by the application user.

This chapter covers the methodology of two aspects, namely the numerical methodologies used in the various aspects of the application and the methodology of the design space exploration of conical PFC shapes by utilizing the application. The numerical methodology concerns all that happens in the ParaPy application and the CFD simulation. This part is split into sections about the construction of geometry (section 3.1), the set up of the CFD domain (subsection 3.2.1), the mesh (section 3.3) and the RANS simulation (section 3.4). The exploitation of the application for the design space exploration is discussed in section 3.5.

3.1. Geometry

This section discusses the definition of the 2D conical PFC geometry in two steps. Firstly, the chosen parameterization is presented and secondly, the mathematical basis that defines the shape based on the input parameters is explained.

3.1.1. Parameterization

The choice of parameterization was mainly driven by the following criteria; flexibility (the ability to access as much of the design space as possible), efficiency (using the least amount of parameters to have as much detailed control over the shape as possible) and physical meaningfulness (the expected significance of the parameter on aerodynamic phenomena).

For example, as duct areas have significant physical meaning in aerodynamic flows and hub-to-tip ratio have been identified as a main PFC performance driver [10], the fan inlet face frontal area and hub-to-tip ratio are chosen in the parameterization rather than the hub- and tip radii. Similarly, the cone contraction ratio is chosen to define how steep the cone contracts towards the BLI propulsor. A higher contraction ratio leads to less wetted area, potentially reducing viscous drag, while it could also cause separation or have other effects on the boundary layer.

The presented parameterization has 26 degrees of freedom. This creates a highly-dimensional design space that may be too large for a single design exploration study. However, components of this shape (intake, cowling, exhaust, fuselage cone and plug) can be studied individually as well. Each of those components has roughly 5 parameters that define their shape.

Figure 3.2 visualises the input parameters in black. Output parameters are shown if they are relevant for the understanding of the figure.

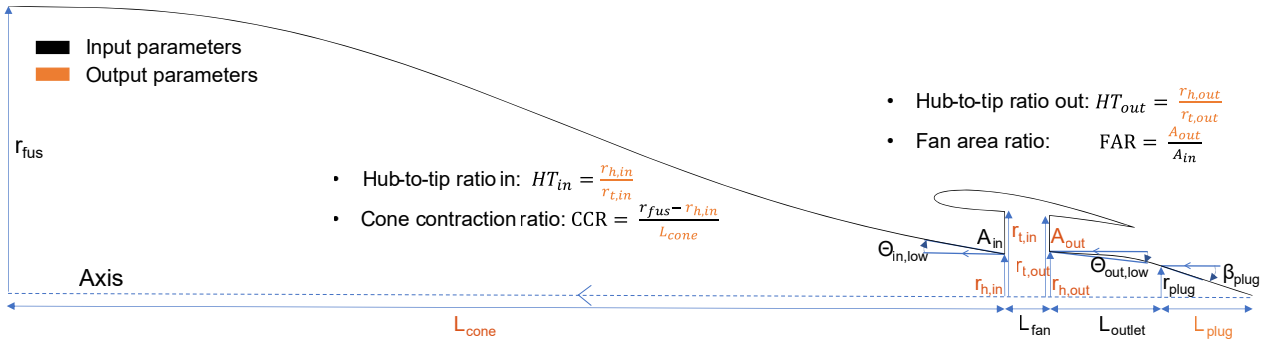

(a) Rear fuselage

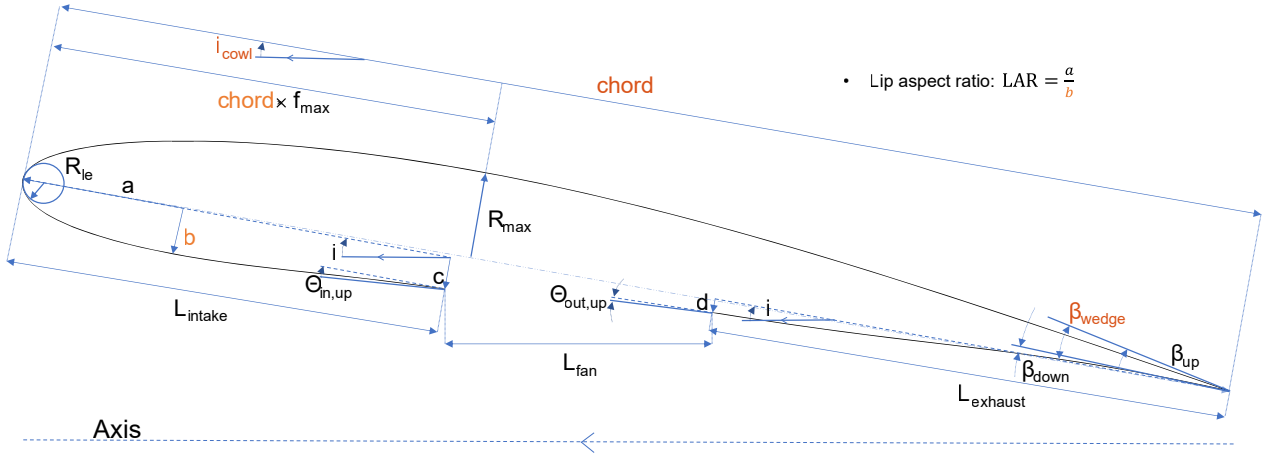

(b) Nacelle

Figure 3.2: Parameterization of the PFC geometry. The black font parameters are user inputs, the orange ones are fully defined by the others.

While the input geometric parameters fully define the geometry, relevant output shape parameters and properties are computed as well; the intake and exhaust duct area distributions, the curvature distributions of each curve, fuselage component volumes, nacelle and fuselage wetted area.

3.1.2. Mathematical curve definition: Class Shape Transformation

The 2D geometry is mathematically defined by Class Shape Transformation (CST) curves [26, 27]. This method is shown to produce suitable curves for aerodynamic design, offering desirable features such as smoothness, flexibility and mathematical efficiency.

CST curve mathematical definition

Constructing the curve in the x-y plane, ζ is defined as the normalized y location and t as the normalized x location, both normalized by the axial length of the curve l.

$$\zeta(t) = C_{N_2}^{N_1}(t) \cdot S(t) \quad ; \quad \zeta = \frac{y}{l} \quad , \quad 0 \leq t = \frac{x}{l} \leq 1 \tag{3.1}$$

The CST curve is a product of a class function $C(t)$ and a shape function $S(t)$. The class function (Equation 3.2a) defines a base shape with known properties, depending on input parameters N_1 and N_2. The shape function modifies this class function without changing its core properties. It does this by means of an n amount of Bernstein coefficients denoted as A_i. Equation 3.2b mathematically defines the shape function.

$$C_{N2}^{N1}(t) = (t)^{N1}(1-t)^{N2} \tag{3.2a}$$

$$S(t) = \sum_{i=1}^{n} A_i \cdot S_i(t) = \sum_{i=1}^{n} A_i \cdot \binom{n}{i} t^i (1-t)^{n-i} \tag{3.2b}$$

The input parameters of the class function N_1 and N_2 are known from the desired geometric characteristic for the considered curve at $t = 0$ and $t = 1$ respectively. However, a disadvantage of shape function input parameters (Bernstein coefficients A_i) is that they do not bear physical meaning, nor are they intuitive indicators of relevant shape properties. Therefore, a translation method between the design parameters and Bernstein coefficients is developed by the author, inspired by the work of Christie et al. [28]:

Translating input parameters to Bernstein coefficients

Writing Equation 3.2a and Equation 3.2b into Equation 3.1, and introducing an expression $T_i(t)$ yields:

$$\zeta(t) = (t)^{N1}(1-t)^{N2} \cdot \sum_{i=1}^{n} A_i \cdot \binom{n}{i} t^i (1-t)^{n-i} = \sum_{i=1}^{n} T_i(t) \cdot A_i \tag{3.3}$$

As $T_i(t)$ contains all variables dependent on t, the derivatives of arbitrary order of the CST curve can be expressed as follows, with m being the order of the derivative:

$$\zeta^{(m)}(t) = \sum_{i=1}^{n} T_i^{(m)}(t) \cdot A_i \tag{3.4}$$

Input parameters in the chosen parameterization can be expressed as a 0th, 1st or 2nd derivative of ζ. Such a constraint can be written in the following form, with b being the value of the constraint defined at t:

$$\zeta^{(m)}(t) = \sum_{i=1}^{n} T_i^{(m)}(t) \cdot A_i = \begin{bmatrix} T_1^{(m)} & \dots & T_n^{(m)} \end{bmatrix} \cdot \begin{bmatrix} A_1 \\ \vdots \\ A_n \end{bmatrix} = [b] \tag{3.5}$$

For multiple constraints, this is extended to a system of equations, in which n constraints are used to solve for the vector A containing the Bernstein coefficients:

$$\mathbf{A} = \mathbf{T}^{-1} \cdot \mathbf{b} = \begin{bmatrix} A_1 \\ \vdots \\ A_n \end{bmatrix} = \begin{bmatrix} T_{1,1}^{(m)} & \dots & T_{1,n}^{(m)} \\ \vdots & \ddots & \vdots \\ T_{n,1}^{(m)} & \dots & T_{n,n}^{(m)} \end{bmatrix}^{-1} \cdot \begin{bmatrix} b_1 \\ \vdots \\ b_n \end{bmatrix} \tag{3.6}$$

The leading radius of a rounded airfoil shape (such as the intake, or cowling) can also be prescribed using this methodology, but this is a special case as it is only a function of the first Bernstein coefficient A_0. Unlike other Bernstein coefficients, A_0 used for the leading edge radius is not a function of others and it is defined as: $A_0 = \sqrt{\frac{2R_{le}}{l}}$ [28].

By solving this system of equations, the Bernstein coefficients A_i are determined and the curve is mathematically defined. This is done for the following geometry segments; the cone, outlet and plug contours (fuselage components) and intake curve, exhaust curve and cowling (nacelle components). One benefit of this translation method is that input parameters can easily be added or removed, if the parameterization is changed.

Example: intake curve

As an example, an intake curve is shown in Figure 3.3. For this curved leading edge curve at $t = 0$ with non-zero at $t = 1$, $N_1 = 0.5$ and $N_2 = 0.0$. The five shown constraints on the intake curve shape are each written in the form of Equation 3.5 and the system of equations of Equation 3.6 is solved for the Bernstein coefficient vector **A**.

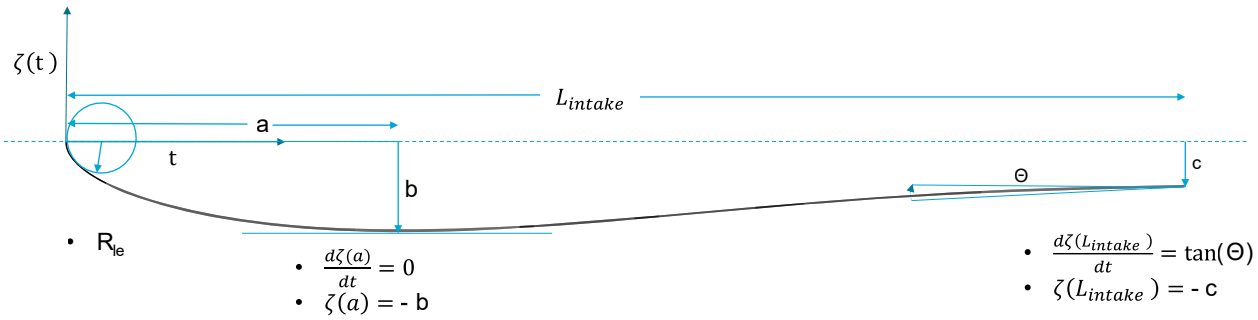

Figure 3.3: Example intake curve as CST curve, shaped by the definition of 5 intuitive input parameters.

3.1.3. Duct area calculation

The intake and exhaust ducts areas are relevant geometric outputs to monitor. The area perpendicular to the flow direction is of interest for aerodynamics, but as the exact flow direction is unknown at the moment of geometry construction, an accurate approximation is searched. It is common to use purely radial definitions of cross-sectional area planes [29]. However, this method becomes increasingly inaccurate with more conical fuselage and nacelle shapes, as the angle between flow and area plane increases. Therefore, the methodology in this study finds the point on the fuselage curve for the minimum cross-sectional area for 100 sampling points on the intake curve and exhaust curve, for the intake and exhaust area distributions respectively.

3.2. CFD Domain and Boundary Conditions

3.2.1. CFD domain

A C-shaped domain (Figure 3.4) was used for the 2D axisymmetric RANS analysis. As the body is axisymmetric around the longitudinal axis and steady flow is assumed in the simulation, axisymmetric flow is assumed. Therefore, only half of the body and domain was simulated to reduce computational effort. The dimensions of the domain are defined as a function of aircraft length and radius. The used domain size was determined to have negligible interference with the solution (see subsection 4.1.1).

The far field boundary condition was imposed on the outer extends of the domain by defining the ambient pressure p_∞, temperature T_∞ and Mach number M_∞. The atmospheric conditions at flight altitude were determined using the ISA model [30]. A no-slip wall condition was imposed on the fuselage and nacelle surfaces.

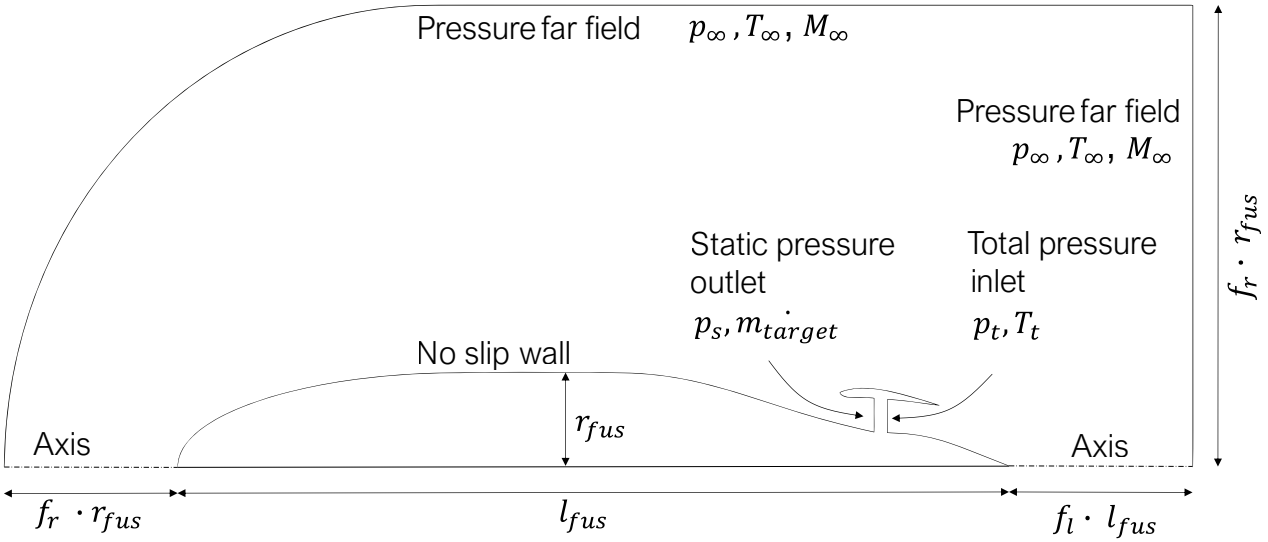

Figure 3.4: CFD domain with boundary conditions and domain dimensions

3.2.2. Fan modeling

The fan in- and outlet faces are modeled by means of the static- and total pressure outlet boundary conditions respectively, as shown in Figure 3.4. These boundary conditions are interlinked and update each iteration. This is facilitated by specifying parametric expressions instead of numerical values for the definition of the boundary conditions. The setup of these boundary conditions is such that the only input parameter is the fan pressure ratio (FPR), defined as:

$$FPR = \frac{p_{t,out}}{p_{t,in}} \tag{3.7}$$

$p_{t,in}$ (area-averaged) is calculated every iteration and in turn used as an input parameter to determine $p_{t,out}$ for the fan outlet face boundary condition. The conservation of mass flow through the fan is imposed by setting a target mass flow condition at the fan inlet face, which equals the mass flow at the fan outlet face. The total temperature at the fan outlet face is derived from the following isentropic flow equation [19], assuming a unity isentropic fan efficiency:

$$\frac{T_{t,out}}{T_{t,in}} = \left(\frac{p_{t,out}}{p_{t,in}}\right)^{\frac{\gamma-1}{\gamma}} \tag{3.8}$$

The implementation of the boundary conditions in Fluent is presented in appendix A.1. In the boundary condition at the fan outlet face, the flow direction is set to be the average of 1) the tangent of the fan outlet face with the nacelle exhaust curve and 2) the tangent of the fan outlet face with the fuselage outlet curve. This is done to account for the flow direction changing with conicity.

Some important simplifications are made in the modeling method of the fan. Firstly, the isentropic fan efficiency is deliberately kept to unity, to reduce complexity and avoid additional assumptions regarding the fan. Secondly, swirl is neglected at the fan outlet, so the exhaust flow has no tangential component, also for simplicity and to avoid additional assumptions. It is estimated that the omission of swirl induces an underestimation of viscous force in drag direction in the exhaust duct and over the plug. Lastly, no in- or outlet guide vanes, structural elements or any other surfaces other than the fan are modeled in the aerodynamic flow.

3.3. Blocking, Mesh and Topology

For the CFD analysis, the domain is to be discretized into a mesh. An automatic structured grid generation methodology has been implemented using the Salome SMESH meshing algorithm supported by ParaPy. In order to have detailed control over the mesh quality and density, the domain has been divided into blocks. This chapter covers the blocking structure, mesh generation and the mesh control methods.

3.3.1. Blocks

The blocks are shaped to facilitate the creation of a C-topology structured grid around both the fuselage and the nacelle. This allows the nacelle and plug geometry to have a sharp trailing edge. The blocks containing the fuselage or nacelle wake are positioned orthogonal to the expected flow direction, and they slightly diverge downstream as a result.

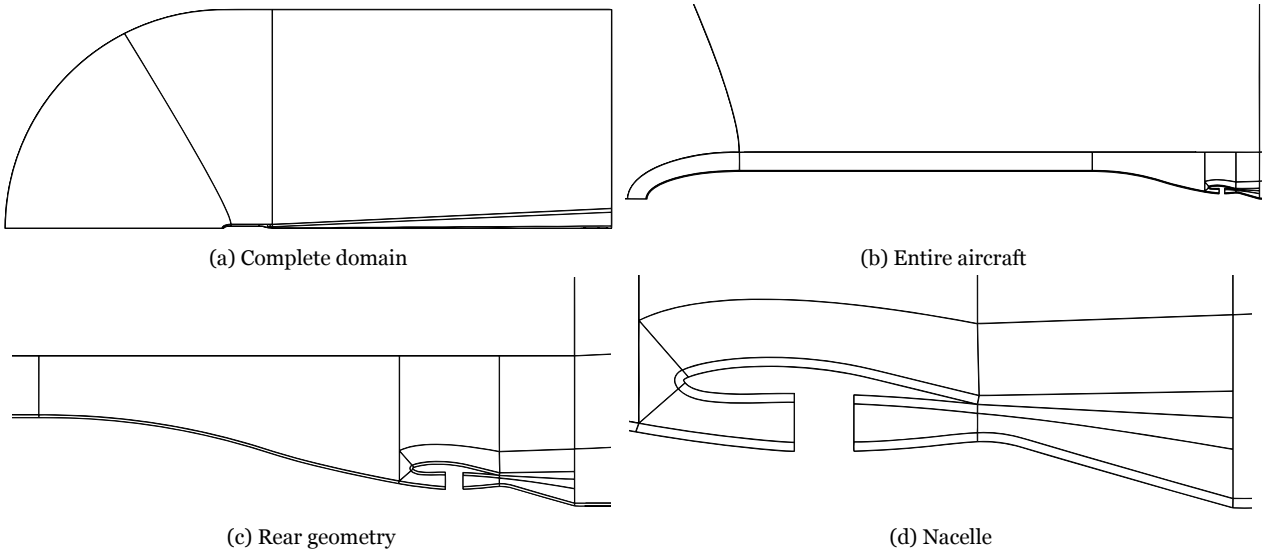

(a) Complete domain

(b) Entire aircraft

(c) Rear geometry

(d) Nacelle

Figure 3.5: Different perspectives on the blocking structure in the domain

3.3.2. Mesh

A structured mesh was made using only quadrilateral mesh cells. The mesh was made as orthogonal and smooth as possible. The mesh density suitable for the mesh was determined through a mesh convergence study (see subsection 4.1.1).

In order to capture the viscous effects in the boundary layer, a sufficiently thin first prism layer was selected, starting from the aircraft surface. The height of the first prism layer (first wall distance y_{wall}) was estimated based on the conventional condition that the $y+$ value remains less than or equal to unity. The first wall distance is estimated based on the ambient density ρ, dynamic viscosity μ and Schlichting's Reynolds number based estimation of the wall shear stress τ_w [31]:

$$y_{wall} = \frac{y^+ \mu}{\rho \sqrt{\frac{\tau_w}{\rho}}} \tag{3.9}$$

Using the above estimator, the first wall distance was set to $3.6\mu m$ around the nacelle and $6.0\mu m$ around the fuselage contour. The resulting $y+$ value was verified to remain below 1 in the simulations (see subsection 4.1.1). Figure 3.6 and Figure 3.7 show pictures of the resulting mesh.

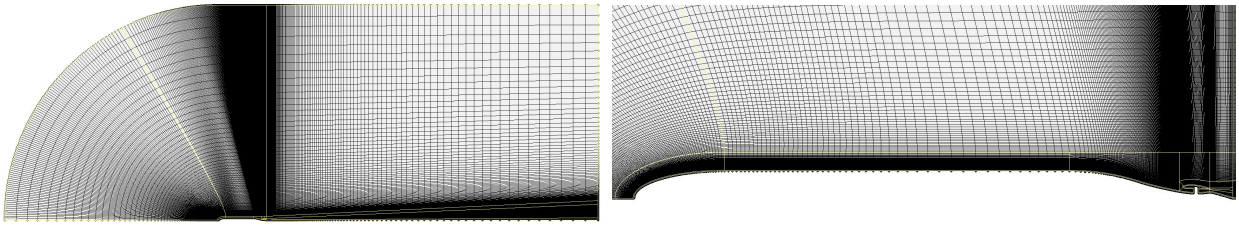

(a) Mesh over complete domain (b) Mesh surrounding aircraft

Figure 3.6: Structured mesh

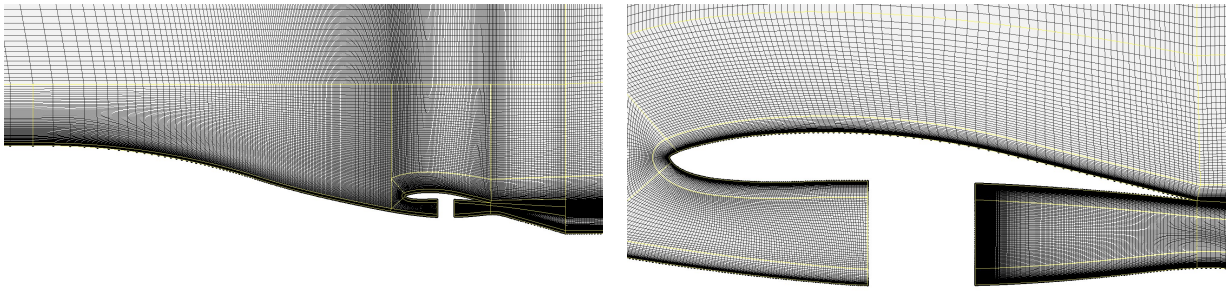

(a) Aircraft rear geometry (b) Nacelle close-up

Figure 3.7: Structured mesh close-up

3.3.3. Mesh controls and tools

The control over the mesh was achieved by imposing mesh controls on the faces and face edges of the domain blocks; structured quadrilateral 2D mesh elements were imposed on all the faces. The following ParaPy mesh control methods were used to control the mesh node distribution on the block edges.

1. *FixedNumber*: a prescribed number of mesh nodes on the edge, with an additional ability to impose a mathematical function describing the node distribution on the edge.
2. *FixedStartEndLength*: a prescribed mesh cell length of the first and last mesh cell length along the edge. Between these lengths, the length of the mesh cells is interpolated. This mesh control method was used to specify the first wall distance.
3. *MaxDeflection*: based on a specified minimum distance x, the mesh nodes' distance to the associated edge cannot exceed x. This method was applied on the leading edge of the nacelle, as the required mesh density strongly depends on curvature.

To streamline the meshing of the domain, the capability to copy mesh controls to opposite edges (an edge lying on the opposite side of the block face) was added. This way, the mesh controls of the opposite edges are overruled. An edge can also be excluded from this, by specifying it as an *autonomous mesh control* edge.

3.4. CFD methodology

The commercially available software package Ansys Fluent 2021 R2 (*Fluent*) was used for the RANS simulation. An automatic script generator was developed to provide Fluent with the required input files from the ParaPy application (a mesh file, a file with simulation settings and a file with procedural commands for Fluent). The simulation could be triggered on the user's local computer, or on a more powerful remote computer located at the TU Delft. In Fluent, the density-based solver scheme was selected, as compressible flow is expected given the free stream flow mach number of 0.78 in this study. To discretize the differential equations of both momentum, energy and turbulent quantities, a second order upwind scheme was used. The fluid was modeled as an ideal gas and the gas

thermodynamic properties are defined by the kinetic theory. Sutherland's three-coefficient law is used for the definition of the dynamic viscosity.

The $k-\omega$ shear-stress transport turbulence model (SST k-ω) was used. Its appropriateness is based on multitude of previous applications regarding analysis of aerodynamic installation of BLI propulsion systems [17, 29]. Domain inlet turbulence intensity was set to 0.1% with a turbulent viscosity ratio of 5.

3.5. Design exploration study

The third research question of this research is to test the hypothesized design direction of increased conicity of the rear-fuselage and nacelle. To answer this question and its sub-questions, the application is exploited in a design space exploration. The third research question consists of sub-questions that collectively provide an answer to the main question. Question 3(a) refers to the direct aerodynamic effect of increasing conicity. Therefore, a conicity parameter sweep is conducted to isolate the effect of conicity on the aerodynamics of the PFC in the specification of APPU.

Question 3(b) refers to emerging design opportunities due to the increased conicity. Emerging opportunities are identified in the conicity sweep. One conical design is chosen to further progress using those design directions. Question 3(c) is answered in the process of answering 3(a) and 3(b). With this information and the comparison to an axis-parallel baseline design, the main conclusion is drawn.

This section contains subsections regarding the construction of that baseline design, the engineering rules bounding the design space to keep the design feasible, and a discussion of the chosen design progression strategy.

3.5.1. Baseline

In order to judge whether or not a design is an improvement relative to an axis-parallel case, a baseline design is required. However, as no proven design with the desired specifications was available, a credible baseline was approached. Therefore, a modified version of the CENTRELINE Rev03 shape was made [32]. However, that CENTRELINE shape was modified to match some top-level-requirements of the APPU project. The modification steps applied on the CENTRELINE shape were based on:

1. *Geometric similarity*; a geometric scaling factor in all directions was applied in order to match the axial length of the APPU baseline aircraft (the Airbus A321 Neo) of 44.5m. This configuration is called "C445" and is shown in Figure 3.8 as the blue contour.

2. *NPF similarity*; NPF similarity was desired between baseline and APPU specification. The desired NPF was calculated from the top level requirement of the APPU BLI fan to produce 10% of total cruise thrust. The estimation of the desired NPF is derived to be $5.13kN$ (see section A.2 for the calculation and underlying simplifications).

   To achieve the desired NPF as defined in Equation 2.9, the drag of the no-BLI fuselage (green contour in Figure 3.8) was determined ($D_{no-BLI,fus} = -9.05kN$) and the NVF was measured in the CFD simulations. Iteratively, the propulsor size scaled to match the target NPF of $5.13kN$. The scaling was performed using the following steps: first, the cone inflection point was found on the original fuselage contour. Then, the geometry downstream of the inflection point was scaled with an additional factor and re-positioned to align with the contour upstream of the inflection point. At last, the curves are connected again by a curve extension at the inflection point. Figure 3.8 shows this baseline geometry as the orange line.

This scaling methodology was chosen to interfere as little as possible with the working of the CENTRELINE Rev03 geometry, such that it can still be counted as a credible baseline. For example, all duct area ratios have remained intact. At the same time, it achieves the desired similarity to the APPU specification. Still, it is realised that the shape of the baseline is modified and originally shaped to operate in a different aerodynamic flow.

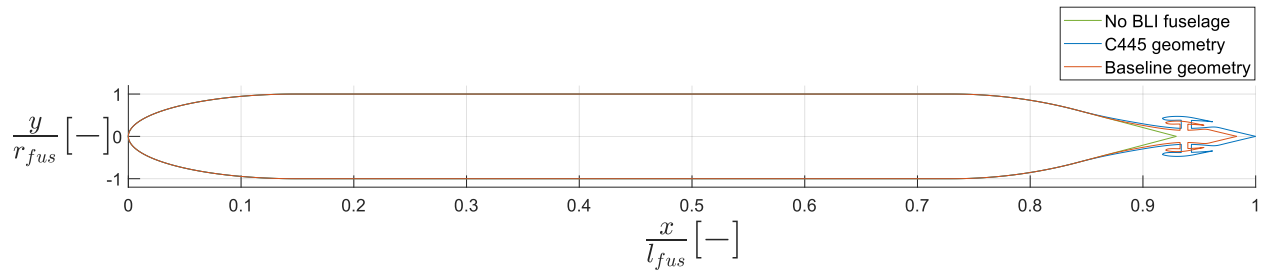

(a) Total overview

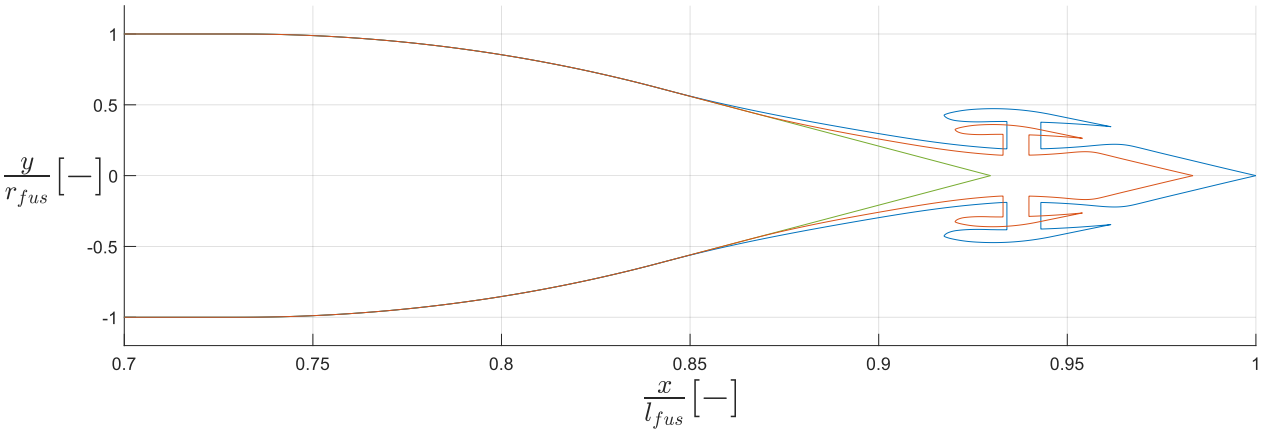

(b) Rear fuselage zoom

Figure 3.8: Contours of the C445, the baseline aircraft and the fuselage with no BLI rear.

3.5.2. Engineering rules as design constraints

This study is focused on aerodynamics during cruise phase only. Therefore, limitations to the design could be overlooked if the design space was unbounded. In order to ensure feasibility in other design disciplines and off-design conditions, rules have been formulated based on literature.

1. *Intake aspect ratio.* The intake has a flow guiding functionality and the omission of this functionality could harm the fan efficiency in high angle of attack or side-slip conditions [33]. This is not taken into account in this study. Therefore, a design trend towards shorter nacelles is expected, as this typically reduces nacelle drag. Peters et al. have studied free-stream short-intake designs and concluded that for intakes with intake length over diameter ratio < 0.25, the benefit from reduced nacelle drag is offset by the reduction in a fan efficiency [33] stemming from reduced flow straightening and increased interaction between fan and a local region of high Mach number. In PFC configurations, the fuselage acts as a flow straightening device and the flow typically has a lower velocity. Still, a rule is set that the intake length over fan blade length cannot exceed 0.5.

2. *Cone volume.* In the proposed APPU configuration, the cone houses a hydrogen fuel tank and other systems. A rule is set that the cone volume cannot be smaller than the baseline cone volume of 55.13 m^3.

3. *Maximum cone angle.* The fuselage cone is to be designed to perform well in off-design conditions such as high angle of attack or angle of side slip conditions. It is expected that the cone contraction ratio can be increased without any separation occurring in cruise conditions, and its most limiting conditions are overlooked in the present study. Therefore, a rule is instated that the maximum angle (measured with the aircraft longitudinal axis) cannot exceed that of the baseline design (17.58°)

4. *Nacelle trailing edge wedge angle.* Based on manufacturing, structural and resulting weight considerations, the nacelle trailing edge wedge angle has to be larger than a limit of 3°.

In case a rule is not satisfied, the geometry representation is invalidated in the ParaPy application. The application user is warned why the design is invalidated and which rules are not satisfied. The user then updates the set of input variables and the design is automatically updated and all rules are evaluated again. If all rules are satisfied, the domain, mesh and simulation interface are available to the user.

3.5.3. Design progression strategy

A design's performance is assessed using all available CFD outputs. The scalar metrics presented in chapter 2 are evaluated for integral performance of the iteration and the convergence fan FPR and mass flow are verified. But also graphs and contour plots of relevant field quantities (Mach number, viscous dissipation, static and total pressure) and reports for fan intake face Mach number are consulted for understanding of the aerodynamic flow field locally. Based on the flow field, changes are made to the input parameters in ParaPy and another design is initiated.

In addition to ambient conditions, flight level and FPR, some shape parameters are taken from the baseline design: fan inlet face area A_{in}, hub-to-tip ratio HT_{in}, fan area ratio FAR, and fan length l_{fan} are copied from the baseline geometry. The fan outlet hub-to-tip ratio HT_{out} and other shape parameters are variable if that is deemed necessary to accommodate the intended shape change. For example, in the conicity parameter sweep, the outlet length L_{outlet} and plug radius r_{plug} were varied to achieve the same nozzle area for designs with different nacelle inclination angles.

4 Model Verification and Validation

4.1. Verification

Three steps are conducted that count to the verification of the model: firstly the domain dimensions varied to see the solution's dependence on domain size. Secondly, a mesh convergence is conducted to measure the interference of the mesh density on the solution. Lastly, it is verified using the y^+ value that the mesh near the wall was sufficiently refined.

4.1.1. Domain and Mesh Convergence Study

In order to eliminate interference from the domain size on the P_{fan} and NPF metrics, three domain sizes were analysed with the same mesh density. The sizes are listed in Table 4.1. The results of this comparison are plotted in Figure 4.1, where the domain size is shown to have a negligible influence on the performance metrics, hence the smallest domain dimensions were chosen.

Table 4.1: Domain sizes

	f_r	f_l	Number of mesh cells ($\times 10^5$)	P_{fan} (MW)	NPF (kN)
1	100	8	2.874	2.709	8.752
2	100	10	3.074	2.709	8.752
3	130	12	3.527	2.709	8.753

A mesh convergence study is performed to verify the model convergence properties. Five different mesh refinement levels were used, ranging between 1.2×10^5 and 5.2×10^5 mesh cells. All the analyses for this mesh convergence study are conducted on the C445 geometry. Richardson extrapolation estimates of the continuum value for two key metrics (P_{fan} and NPF) are calculated with the finest three meshes to show that the model converges to a reasonable value as the mesh is infinitely refined. The refinement was increased progressively for the five meshes: a mesh density scaling factor was used to achieve a uniform refinement. However, all first wall distances have remained the same and such that y^+ stays below unity for every mesh density.

Mesh convergence results for NPF and P_{fan} are shown in Figure 4.1. The three finest meshes align linearly, which is expected from the second-order method in two dimensions. The two coarsest meshes do not follow this trend and are deemed too coarse to yield accurate results. Based on this mesh convergence study, the mesh with 2.9×10^5 cells is used throughout this research. Both continuum values based on the Richardson extrapolations shown in Figure 4.1 show a difference with the values from the chosen mesh density of only 0.38%, making it a very suitable mesh density for this application.

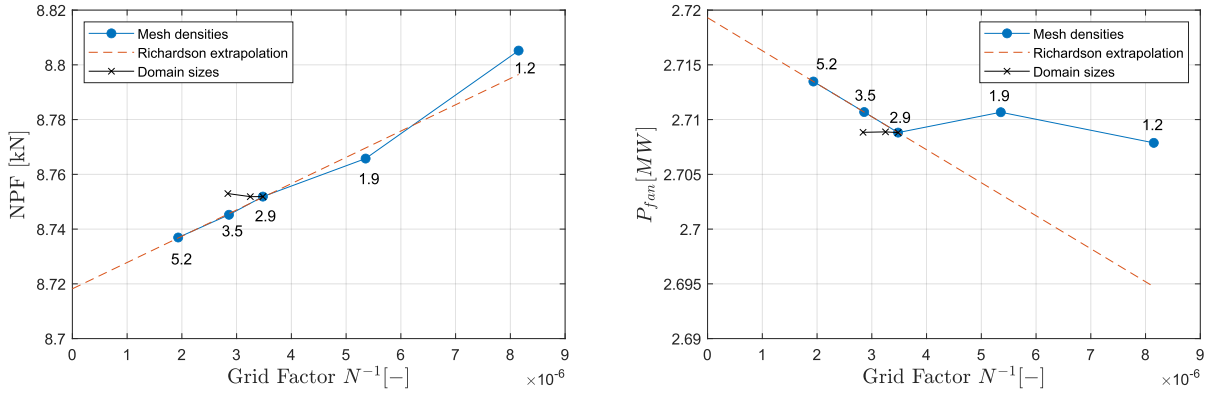

Figure 4.1: Mesh convergence plots with Richardson extrapolation of the three finest meshes. The number annotations in the graph indicate the number of mesh cells (times 10^5)

4.1.2. Mesh refinement near the wall

As a last verification step, it is verified that the mesh is sufficiently fine near the walls to obtain a y^+ value below 1, indicating that the boundary layer is fully resolved.

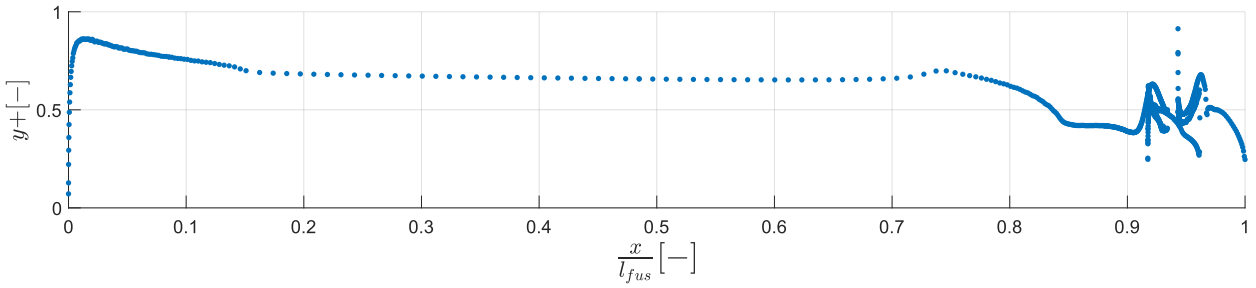

Figure 4.2: y+ values of the C445 geometry as verification of the used first wall distance

4.2. Validation

Now that the domain and mesh are verified, the validation step is conducted to assess the validity of the meshing and CFD routine. Seeing how the outcomes of this work's methodology compare to that of a higher-fidelity method builds confidence in the accuracy of this model and it could point at required model improvements.

4.2.1. Validation set up

The meshing and simulation methods were validated to those used by Van Sluis et al. in 2D axisymmetric numerical simulations in the context of the CENTRELINE study [32]. The validation was conducted by comparing the simulation outcomes by Van Sluis et al. of the Revo3 geometry to the routine of the present study, with the same geometry and ambient conditions. While similarity is found in simplifications on fan efficiency and swirl, there are important differences.

The main difference is that Van Sluis et al. used a body force model to model the fan, adding axial momentum to the flow, where the present study models the fan by means of boundary conditions specifying FPR. Also the solver types are different, which could cause differences in compressible flows. The similarities and differences in the methods between the present study and validation study by Van Sluis et al. [32] are listed in the table below:

Table 4.2: Methods used in the validation and present study to overview similarities and differences

Same		Different		
			Present study	Validation study
Geometry	Rev03	Fan modeling	Boundary conditions	Body Force Model
Fan efficiency	1	Solver type	Density based	Pressure based
Fan swirl	None	Discretization scheme	2^{nd} order upwind	MUSCL (3^{rd} order)
Domain shape	C-shaped	Domain size	$f_l = 10$ $f_r = 100$	$f_l = 15$ $f_r = 300$
Turbulence model	SST $k-\omega$	Air model	Kinetic theory	Ideal gas
Ambient conditions	ISA + 10 FL350 M = 0.80			
FPR	1.40			

4.2.2. Discussion of the comparison

The table with CFD solution variables is presented in Table 4.3. The value for $D_{no-BLI,fus}$ needed for the calculation of NPF was unknown. Based on the $D_{no-BLI,fus}$ = 37.61kN value presented by Van Sluis et al. for Mach 0.82 conditions [32], the NPF was calculated with an estimated $D_{no-BLI,fus}$ = 35.0 kN for this comparison in Mach 0.80.

Table 4.3: Comparisons between simulations by Van Sluis et al. [32] and present study.

Solution variable	Present study	Validation study	Δ [%]
$\dot{m_{fan}}$ [$\frac{kg}{s}$]	200.19	202.17	-0.978
NPF [kN] ($D_{no-BLI,fus}$ = 35.0kN)	34.3	33.8	1.5
P_{fan} [MW]	5.036	5.206	-3.27
IPR [%]	98.975	98.932	0.043
FPR [-]	1.4000	1.3969	0.222
$T_{t,in}$ [K]	256.54	253.53	1.19
$T_{t,out}$ [K]	282.43	278.98	1.24
M_{in} [-]	0.579043	0.5865	-1.27
M_{out} [-]	0.404167	0.4053	-0.280

Table 4.3 shows the two studies agree in a range of 3.3% for all solution variables. However, some differences can also be observed; firstly, the mass flow through the fan is slightly underpredicted in the present study, which contributes to the underprediction of fan power. However, while this is expected to lead to an underprediction in NPF as well, an overprediction is observed.

Secondly, an underprediction of total temperatures is observed at the fan in- and outlet faces is observed. However, while the slightly underpredicted fan inlet face Mach number is expected to lead to a lower value for the total temperature there, a total temperature overprediction is seen. Given the same ambient conditions, this is unexpected. The ratio of total temperatures at fan inlet and outlet is the same for both studies.

The main cause of these discrepancies lies in the different methods of fan modeling methodologies between the two studies; the fan boundary conditions used in the present study impose a flow quantity uniformly on the boundary. For example, total temperature and total pressure are imposed uniformly on the fan outlet face. This is not entirely physical and this is a major difference compared to the body force fan model used by Van Sluis et al. where non-uniform profiles of these quantities exist at the fan in- and outlet. The difference in total pressure profile on the fan inlet and outlet face is shown in Figure 4.3. Looking at the total pressure contours for the validation study in Figure 4.4, clear total pressure layers are seen in the exhaust duct, where these are non-existent using the present methodology.

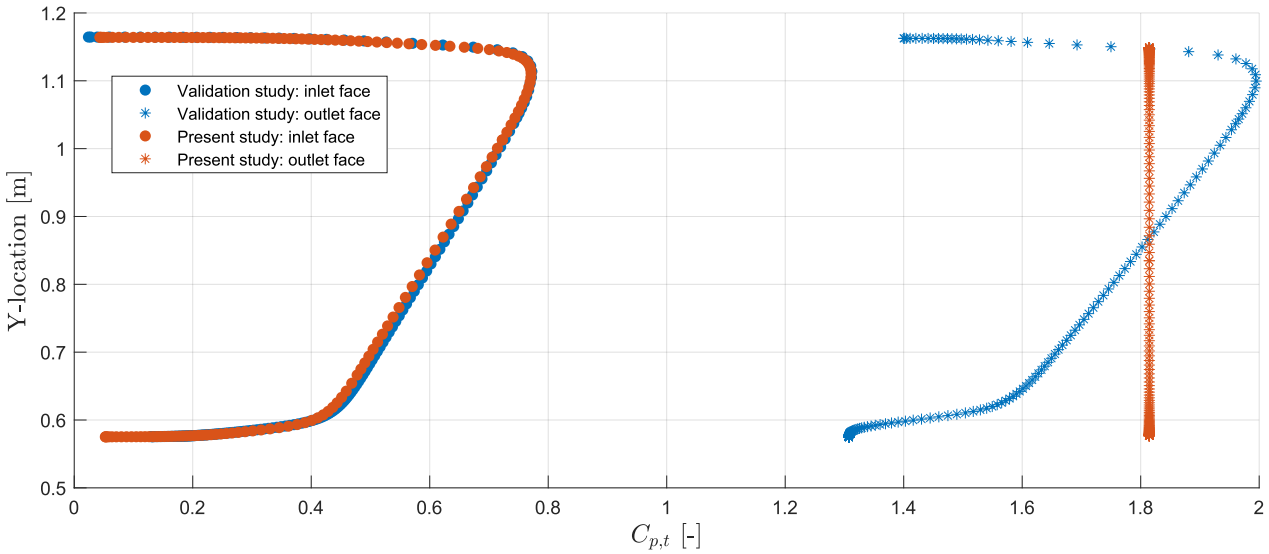

Figure 4.3: Total pressure profiles at the fan inlet and outlet face, comparing validation and present study.

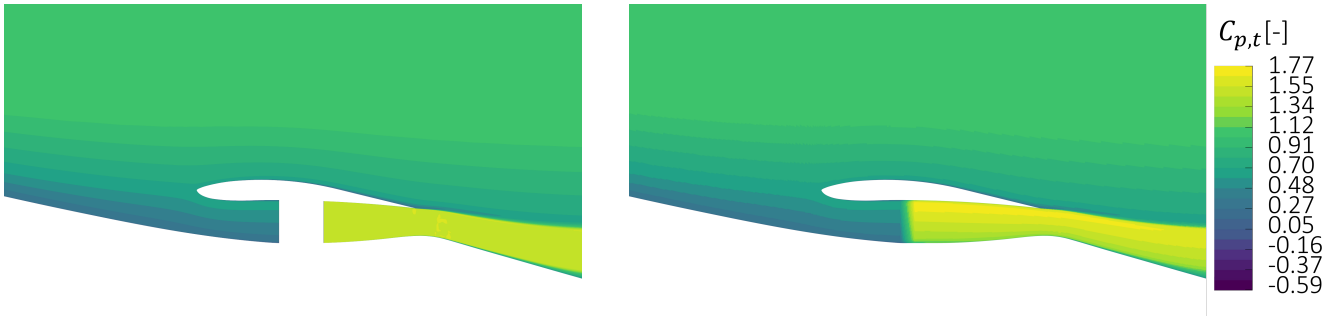

(a) Present study

(b) Validation study

Figure 4.4: Total pressure contour around the validation design

Conclusion

While there are differences in the solution between the present study and validation study, all relevant solution variables agree within a range of 3.3%. While the differences can be explained, the presented application is deemed accurate enough to conduct design space explorations.

5 Results and Discussion

The verified and validated application is utilized to explore the design space of conical PFC shapes, to prove or disprove the hypothesis that increasing conicity could benefit the aerodynamic efficiency of PFC shapes. First, a conicity parameter sweep is conducted, to isolate its aerodynamic effect.

5.1. Conicity parameter sweep

Using input parameters i, $\Theta_{in,low}$, $\Theta_{out,low}$ and HT_{out}, the conicity was incremented, keeping all other input parameters constant. While conicity concerns all four parameters, nacelle inclination angle i is used to indicate the design's level of conicity. For similarity, A_{in}, HT_{in}, FAR and cone contraction ratio CCR were copied from the baseline design. A first design ($i = 6°$) was made to match the intake and exhaust duct area distribution of the baseline design. From there on, the conicity was incremented to $i = 15°$. The nozzle plane cross-sectional area A_{nozzle} was also kept constant, attempting to control fan mass flow. Figure 5.1 shows the contours and duct area distributions.

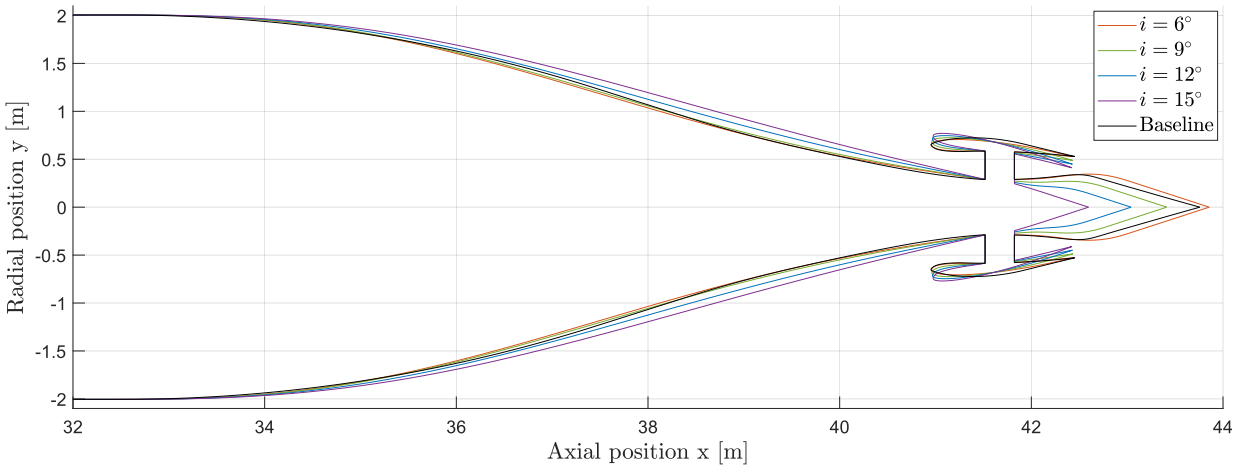

(a) Contours of the rear fuselage and BLI installation.

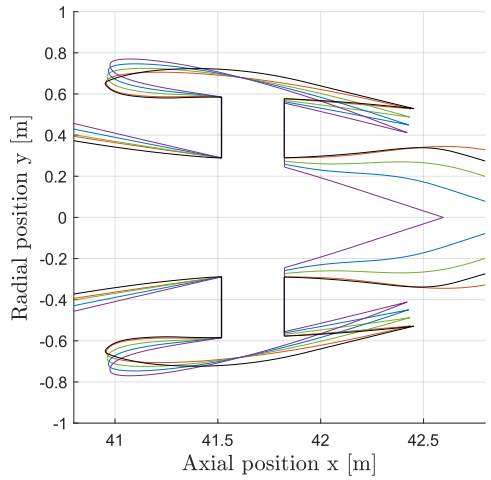

(b) Nacelle contour detail

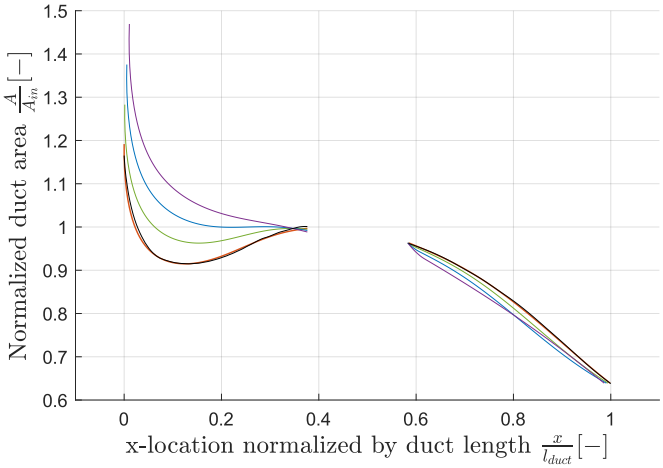

(c) Area distributions in the intake and exhaust duct.

Figure 5.1: Contour and area distribution development for designs with increasing conicity

Several geometric developments stand out while increasing conicity. Firstly, the plug shrinks a lot for a similar exhaust area distribution. As the nacelle trailing edge moves radially inward, the plug has to move even more inward to achieve the same nozzle area, thereby quickly reducing the size and convexity of the plug geometry. The conicity could not increase further than $i = 15°$, or the plug would completely disappear and the desired nozzle area could not be realized.

Secondly, the fuselage cone gains volume and wetted area with conicity, which is caused solely by the increasing $\Theta_{in,low}$ parameter. This is shown in Table 5.1. The table also shows the total wetted area $A_{wet,total}$, which is mainly influenced by a growing cone, but shrinking plug.

i [°]	6	7	8	9	10	11	12	13	14	15
$V_{cone}[m^3]$	55.48	56.17	56.87	57.58	58.31	59.05	59.81	60.59	61.94	62.19
$A_{wet,total}[m^2]$	467.3	468.3	469.0	469.7	471.6	473.6	474.0	474.2	473.2	469.9
$A_{wet,cone}[m^2]$	86.38	87.04	87.70	88.37	89.04	89.72	90.40	91.08	92.25	92.47
$A_{wet,nacelle}[m^2]$	10.49	10.45	10.42	10.40	10.37	10.34	10.31	10.29	10.26	10.24
$A_{wet,plug}[m^2]$	3.14	2.61	2.24	1.99	1.72	1.48	1.24	1.03	0.840	0.634

Table 5.1: Geometric properties cone volume and wetted area in the conicity sweep

Lastly, Figure 5.1c shows the area distribution in the intake and exhaust ducts resulting from the conicity sweep. Looking at the intake, the contraction from the highlight plane to the fan intake face is increasing and the subsequent region of diffusion is reduced for increased cone angles. Beyond 12°, the intake duct area is monotonically decreasing, meaning the duct is only contracting. This implies no throat point upstream of the fan and no flow diffusion in the intake duct.

5.1.1. Integral aerodynamic performance

The integral aerodynamic performance of the designs is shown in Figure 5.2 plotting P_{fan} versus NPF. Each design's conicity level is indicated using nacelle inclination angle i. Also indicated is the line of 10% of total cruise thrust. Also, an example design is shown in a FPR sweep, plotted in green. This shows a linear trend between P_{fan} and NPF and this trend is also plotted for comparison.

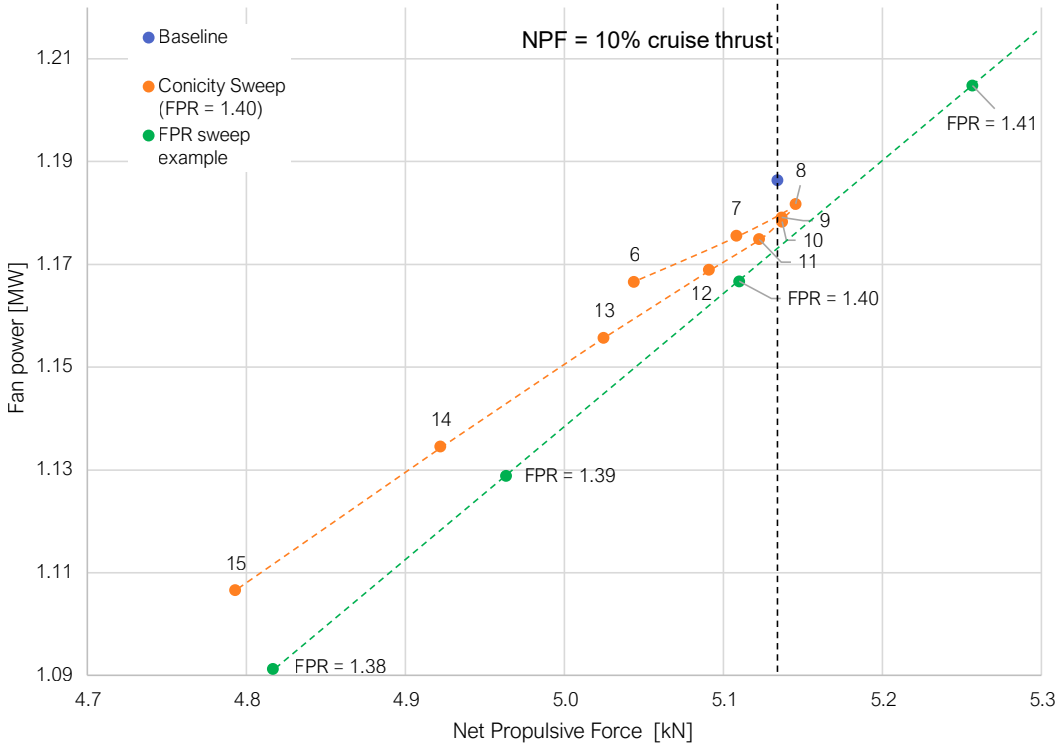

Figure 5.2: Fan power versus net propulsive force for the conicity parameter sweep (orange) and FPR sweep (green). Indicated are nacelle inclination angle i (orange points) and FPR (green points).

As fan power is minimized for a given NPF, designs in the lower right section of Figure 5.2 are desirable. From 6° to 8°, the trend line slope is shallower compared to FPR line, indicating a more favorable trade-off in power and force. Beyond 8°, the mass flow rate starts to decrease (see Figure 5.3a), resulting in a reduction in both fan power and NPF. But still, the aerodynamic efficiency increases; from 9° to 10°, the design has a slightly lower fan power for the same NPF. However, beyond 11°, increased conicity leads to a less favorable trade-off of power and force compared to the FPR trend line. Let us try to understand and decompose these trends in the coming sections.

Viscous dissipation

In Figure 5.3a, a continuously decreasing viscous dissipation term is observed. From i of 6° to 15°, the viscous dissipation percentage decrease is around 0.87%. This is a considerable decrease, given the viscous dissipation is computed over the entire domain. This means this figure includes all viscous dissipation losses over the entire fuselage forebody. Also, the total wetted area increases over that range, which typically leads to increased viscous dissipation.

Total pressure in the captured stream tube

To assess the efficiency with which the flow ingested by the fan is treated, Figure 5.3b gives insight in the total pressure losses in the flow before the fan. The fan inlet face total pressure increases up to 11° indicating fewer losses happen upstream in the combination of fuselage and intake. This is worth remarking, especially given the increasing wetted area of the cone shown in Table 5.1, which typically increases total pressure loss. The causes of the trend in total pressure at the fan face are discussed after the trend of fan mass flow rate with conicity level is explained.

Fan mass flow rate

The trend of fan mass flow rate with conicity level observed in Figure 5.3a is caused by the superimposing of two trends: the first is that while the flow direction becomes more conical, the fan stays perpendicular to the longitudinal fuselage axis. Therefore, the angle between flow direction and fan increases with conicity. This effectively decreases the duct area at the fan because the projected fan area in the direction of the flow is decreased. This scales the effective duct area by the cosine of the angle between fan and flow so this phenomenon is more pronounced at higher angles. This phenomenon can also be observed in Figure 5.1c, where the duct area at the fan inlet face decreases with conicity.

The other trend is the total pressure in the captured stream tube at the fan inlet face. Total pressure loss decreases mass flow rate as that comes at the cost of velocity or static pressure, both of which scale with mass flow rate. These trends oppose each other up to 11° conicity, and reinforce eachother in decreasing the mass flow rate beyond 11° conicity.

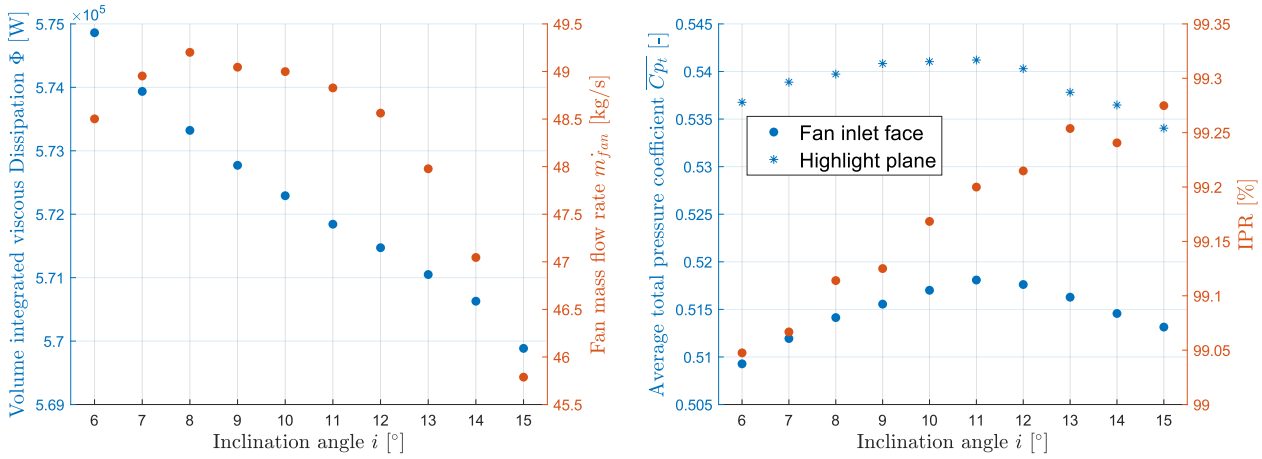

(a) Viscous dissipation and mass flow

(b) Highlight plane and fan inlet face total pressure and IPR

Figure 5.3: Variation of aerodynamic performance indicators with conicity.

There are two more trends visible in Figure 5.3b; the highlight plane total pressure gives indicates the total pressure losses upstream of it and the IPR reflects the intake total pressure loss.

Intake pressure recovery It is observed that IPR increases continuously with conicity. This has causes that are induced by the increased conicity. Firstly, the expansion of the intake duct is lessened as an effect of increased conicity. Flow diffusion in the intake, which associated with irreversible total pressure losses, is thereby reduced. However, diffusion is increasingly moved upstream due to an increasing adverse pressure gradient upstream of the highlight caused by the increasing highlight area. Figure 5.4a confirms the increasing static pressure rise at the highlight plane with increased conicity and this causes diffusion to occur before the highlight plane. Therefore, the diffusion losses are reflected in the highlight plane total pressure.

Secondly, the flow is turned less in the intake for higher conical angles. Changing the flow's direction leads to centrifugal forces and non-uniform velocity profiles. As viscous losses scale with the square of velocity gradients, total pressure is lost there to friction and turbulence. So lessening the turning of the flow is beneficial for the intake total pressure recovery as well. This effect can be attributed to a more efficient intake due to increased conicity.

Highlight plane total pressure The highlight total pressure line in Figure 5.3b indicates the total pressure losses upstream of the highlight plane. As described, this is not only affected by the fuselage, but also by the upstream effect of the intake. The highlight total pressure peaks at 11°. Up to 11°, the increasing trend can be caused by the reduced curvature of the fuselage, both in the convex and the concave sections, which induces less losses due to smaller velocity gradients. Beyond 11°, the increasing wetted area of the cone could dominate this effect and cause an increase of total pressure losses upstream of the highlight plane.

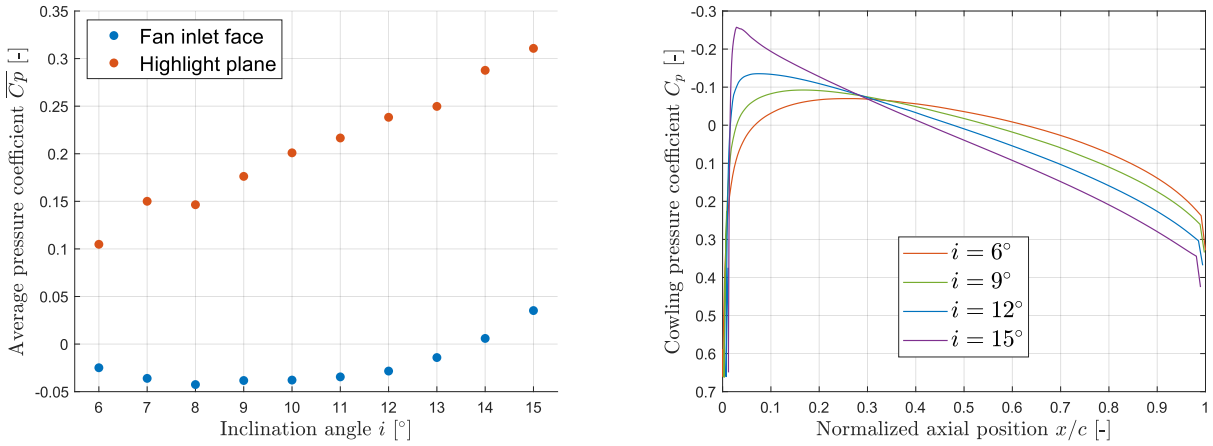

(a) Static pressure coefficient at highlight plane and fan inlet face

(b) Cowling pressure distribution

Figure 5.4: Variation of aerodynamic performance indicators with conicity.

Cowling As shown, the highlight plane area increases with conicity in this parameter sweep and this causes an increased adverse pressure gradient at the highlight plane. This observation is in agreement with the observation in Figure 5.5 that the stagnation point on the intake lip moves radially inward, which means that the captured stream tube expands more towards the highlight. The stagnation point that moves radially inward and the increased nacelle inclination angle change the curvature experienced by the flow going around the cowling. The effect on the cowling's pressure distribution is shown in Figure 5.4b. Here it is seen that the suction peak near the tip and the following adverse pressure gradient increase with conicity. This causes higher acceleration and peak supervelocities over the cowling, which could cause some extra friction losses, but the suction peak is too low to expect any shocks. However, Table 5.2 shows a reducing viscous force in the drag direction, possibly due to the tilted angle of the friction force vector.

i = 6° (a) i = 12°

Figure 5.5: Static pressure contours for two levels of conicity. Both designs have the same fan mass flow rate

i [°]	6	7	8	9	10	11	12	13	14	15
-$F_{x,visc}$ [N]	121.4	120.5	119.1	117.3	115.5	113.5	111.4	109.1	106.2	103.9

Table 5.2: Force in negative axial direction (drag direction) due to viscous friction on the cowling.

5.1.2. Local aerodynamic performance

The viscous dissipation contour plots of Figure 5.6 can be used to localize losses and trends in the flow field; firstly, these plots show a reducing zone of high viscous dissipation in the intake. Secondly, a region of increased viscous dissipation is observed in the flow over the cowling. Lastly, the figure shows strongly reducing viscous dissipation in the jet flow. As a result of the spectacular decrease of plug size and convexity, the flow is accelerated less over the plug, leading to lower Mach numbers (as seen in Figure 5.7). This induces much lower velocity differences with the much slower wake flows formed at the nacelle trailing edge, meaning that the velocity gradients between jet flow and the wakes of the nacelle and fuselage plug are reduced. As shown in Equation 2.13, the viscous dissipation scales with the square of the velocity gradients in the flow. Therefore, the reduced acceleration over the convexity of the plug contributes very effectively to the reduction of viscous dissipation.

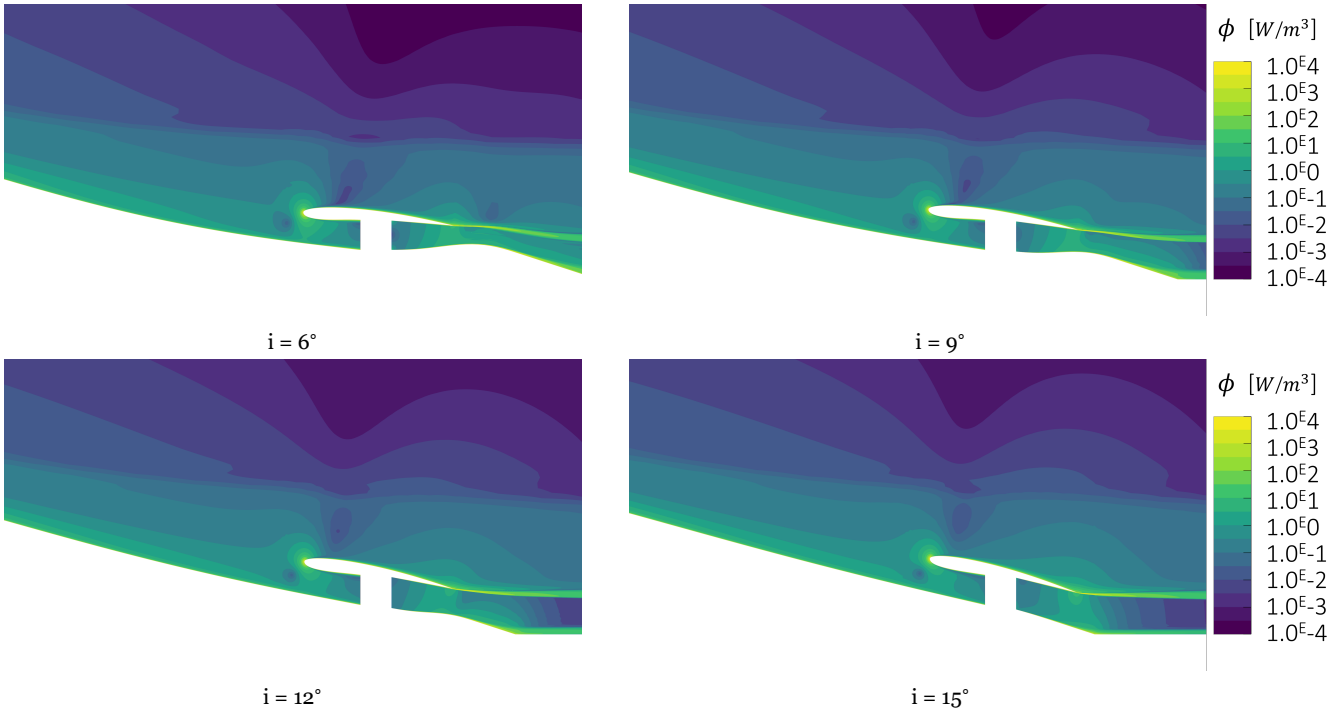

i = 6° i = 9°

i = 12° i = 15°

Figure 5.6: Viscous dissipation contours of the conicity sweep.

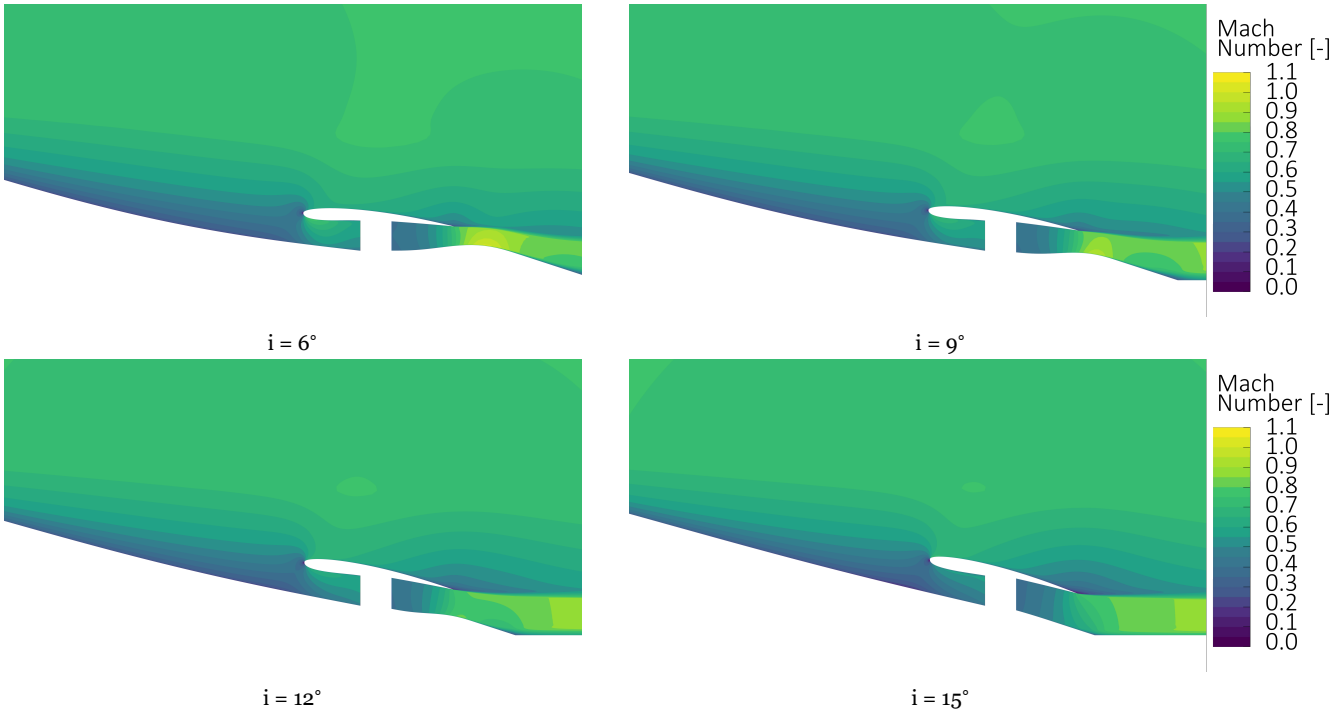

Figure 5.7: Mach number contours of the conicity sweep.

Conclusion

Judging from the fan inlet face total pressure shown in Figure 5.3b, the design with $i = 11°$ has the least total pressure loss of the designs in the conicity sweep. Therefore, this design is chosen for further development. Outside of this conicity parameter sweep, it is called by its name: *A23.5*. To compare the fan power figure for the desired NPF of 10% cruise thrust, the fan pressure ratio is varied such that the fan power at desired NPF can be interpolated. The interpolated fan power is 0.81% lower compared to the baseline design.

5.2. Emerging design opportunities

In addition to direct aerodynamic effects, increased conicity also has emerging geometric effects that present opportunities for further shape improvements. This chapter discusses two: shortening the fuselage by increasing cone contraction ratio, and shortening the intake duct. The effects of these two design directions are demonstrated by means of design progression based on design A23.5. However, no design optimization is conducted and the two discussed design directions are not the only ones with the potential to improve the design. However, they are a geometric implication of increased conicity and can therefore be categorized as indirect effects of increased conicity.

5.2.1. Increasing cone contraction ratio: design A24

As seen in Table 5.1, the volume of the cone increases with conicity. In the APPU design, this volume is valuable as it houses a hydrogen fuel tank. A bulkier design, accomplished by increasing conicity, could therefore be desired. Equally, if a given tank volume in the cone suffices, the fuselage could be shortened. This reduces wetted area and therefore viscous drag and could potentially alleviate the rotation problem at take-off. This logic underlies design A24. Design A24 is the same as A23.5, except for the cone contraction ratio that is reduced by 4.2%. This effectively shortens the fuselage, while still complying with all design rules discussed in subsection 3.5.2.

5.2.2. Shortening intake duct: design A27

Another design direction is that the intake duct is shortened. There is room within the design rule regarding intake aspect ratio to shorten the intake and as the diffusing functionality has become redundant in the considered flow field, the need for a long intake is lessened. Furthermore, the

highlight area is reduced as a result of the shorter intake, which could reduce the adverse pressure gradient before the intake. With this logic, design A27 is made. Design A27 copies most of design A24, but it has a 29% shorter intake duct. The nacelle keeps the same thickness.

5.2.3. Geometries

The geometries of both A24 and A27 are shown in Figure 5.8. From Table 5.3 it can be seen that the cone resulting from the increased contraction ratio reduces in both volume and wetted area. And as only the discussed parameters have varied, there is a lot of geometric similarity between the designs.

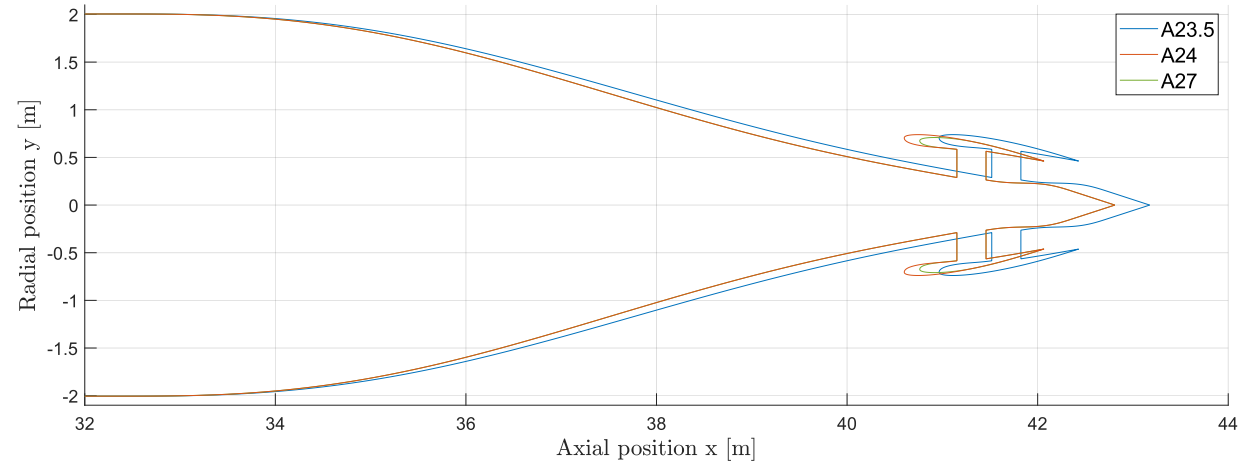

(a) Contours of the rear fuselage and BLI installation.

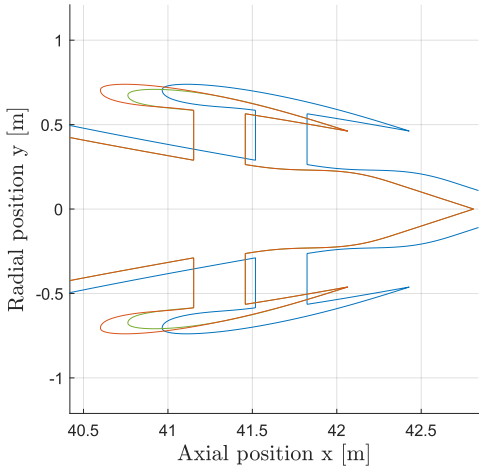

(b) Nacelle contour detail

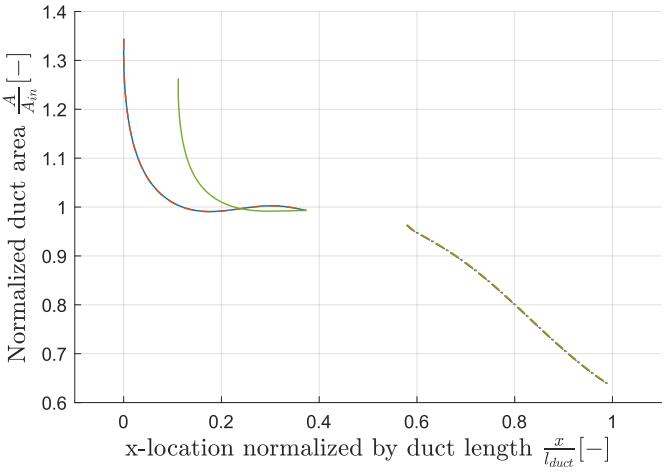

(c) Area distributions in the intake and exhaust duct.

Figure 5.8: Contours and area distributions for designs with a higher contraction ratio and shorter nacelle.

Design	i [°]	Cone contraction ratio [-]	l_{intake} [m]	V_{cone} [m^3]	$A_{wet,cone}$ [m^2]
Baseline	~6	0.1872	0.5652	55.13	86.52
A23.5	11	0.1872	0.5652	59.05	89.72
A24	11	0.195	0.5652	56.30	86.40
A27	11	0.195	0.4000	56.30	86.40

Table 5.3: Geometric data of design A24 and A27, with the reference of the baseline design and A23.5

5.2.4. Aerodynamic performance

The aerodynamic performance is shown by means of a graph displaying fan power versus net propulsive force. The plot contains many analysed design points in orange. The highlighted designs A23.5, A24 and A27 are shown as green dots and the green dashed line indicates the linear interpolation between two incrementally different fan pressure ratios. Table 5.3 shows interpolated values at the NPF corresponding to 10% of cruise thrust.

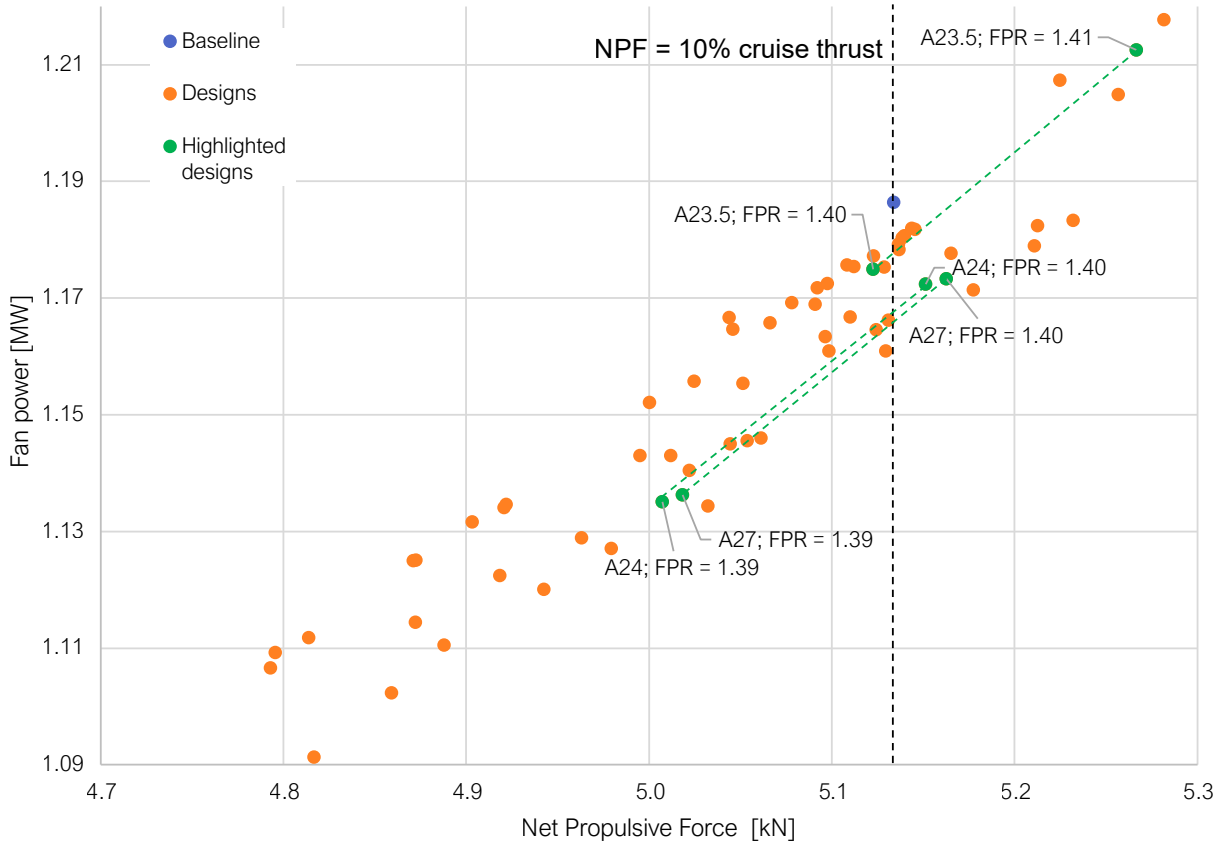

Figure 5.9: Fan power versus net propulsive force for the shortened fuselage and shortened intake designs.

Design	P_{fan} [MW]	ΔP_{fan} [%]	IPR [-]	FPR [-]	$\dot{m}_{fan}$ [kg/s]	M_{in} [-]	Φ [MW]
Baseline	1.186	-	99.128	1.40	49.481	0.571	0.5763
A23.5	1.177	-0.81	99.200	1.4005	48.852	0.562	0.5718
A24	1.167	-1.65	99.204	1.3985	48.646	0.560	0.5694
A27	1.165	-1.81	99.326	1.3977	48.632	0.559	0.5677

Table 5.4: Aerodynamic results of the designs with a shorter cone and a shorter intake duct. ΔP_{fan} indicates the percentage difference between P_{fan} of the design compared to the baseline design.

A24 Judging from the Table 5.4, the 0.81% fan power decrease observed from baseline to A23.5 has doubled progressing to design A24 (1.65% fan power decrease). As much of the shape is the same, the behaviour in the flow field is not much different so the explanation of that gain most likely lies in the wetted area reduction. Therefore, a significant aerodynamic efficiency gain is caused by making the fuselage shorter. This is an indirect effect of the increased conicity, as this creates the potential to shorten the fuselage without reducing the cone volume.

A27 Looking at the 1.81% fan power decrease from shortening the intake duct, the shortened intake shows a small aerodynamic efficiency gain. The intake pressure recovery benefits from the shorter intake, which is expected as the decreased intake area induces less irreversible losses in the intake flow. The viscous dissipation term has reduced as a result. This is also recognized in Figure 5.10, which shows a similar picture for both plots.

A24 A27

Figure 5.10: Viscous dissipation contours of design A24 and A27

6 Conclusions and Recommendations

6.1. Conclusions

An engineering design application was developed that automates the routine for numerical simulation of the aerodynamic performance of axisymmetric propulsive fuselage concept (PFC) designs. The routine comprises parametric geometry generation based on a proposed parameterization, an automated structured multi-block mesh generation and automatic numerical CFD (RANS) simulation.

A parameterization of the 2D geometry of the BLI installation was proposed that proved flexible enough to define well-performing axis-parallel and conical PFC geometries. A mathematical translation from those parameters to the aerodynamically useful CST-curve was developed and used to mathematically define the geometry.

The domain size and mesh density were verified by means of a mesh convergence study. Furthermore, the meshing and simulation routines were validated using a status-quo design by Van Sluis et al.[32], which showed reasonable agreement on all performance indicators. The difference in fan power and net propulsive force is mainly explained by the difference in fan modeling methodologies.

The use of the application has been demonstrated by exploiting it in a design space exploration. The goal of the design space exploration was to test the hypothesis that increasing conicity could improve the aerodynamic efficiency, defined as the required fan power for a given net propulsive force. The design space was bounded by engineering rules from off-design conditions and other engineering disciplines than aerodynamics. These rules constrained the intake aspect ratio, fuselage cone volume, maximum cone angle and nacelle trailing edge wedge angle.

A parameter sweep was conducted to isolate the effect of conicity on the design's flow field and aerodynamic efficiency. This parameter sweep showed a continuous reduction in required fan power and viscous dissipation with increasing conicity level. The total pressure recovery of the captured stream tube initially increased with conicity level, but beyond 11° the opposing effect of increasing wetted decreased the total pressure recovery. The design with 11° conicity level (*A23.5*) showed a 0.81% aerodynamic efficiency improvement relative to a baseline derived from the previous CENTRELINE project with less conicity.

That improvement was partially caused by less intake duct losses. The intake showed an increased intake pressure recovery figure, due to the reduced need to turn the flow and due to the monotonically contracting intake, which eliminated the flow diffusion in the intake. These two aspects contributed to lower intake total pressure loss.

Additionally, the plug size and convexity decreased as a result of the increased inclination angle of the nacelle, while preserving exhaust duct cross-sectional areas. This strongly reduced the flow acceleration and velocity over the plug geometry. This reduced the velocity gradient between this flow and the low velocity wake flows of the nacelle and plug geometry. This significantly contributed to a reduction of viscous dissipation in the jet flow.

With increased conicity, the fuselage cone volume and wetted area were found to increase. This presented the opportunity to shorten the cone without reducing the fuselage cone volume nor exceeding the maximum rear fuselage contour angle of the baseline design. This resulted in a design with a 4.2% shorter fuselage cone (called design A24) that showed a 1.65% aerodynamic efficiency increase relative to the baseline geometry, mainly due to reduced wetted area.

As the intake duct of design A24 was no longer diffusing the intake flow and the guiding functionality of the intake was ensured by the design space bounds, a 29% shorter intake duct was tested. The performance improvement increased to 1.81%, due to the increased intake pressure recovery.

Overall, it is concluded that for PFC configurations with similar aircraft and propulsor scales to the APPU specification, increasing the conicity of the rear fuselage and nacelle could contribute to achieving higher aerodynamic efficiency in cruise conditions.

6.2. Recommendations

To improve the accuracy, credibility and usability of the model, the following is recommended:

- Improve the aerodynamic simulation accuracy by developing a more detailed fan model that can impose or amplify radial profiles of flow quantities such as total pressure and temperature.
- Introduce a swirl component for more accurate modeling of plug aerodynamics. Omitting the swirl leads to an underestimation of drag over the plug.
- Study the effect of the radial inflow due to the conical design on the fan efficiency.
- Using the power balance method on control volumes of interest (intake-, exhaust- or jet flow to name a few), a future study could decompose, localize and quantify where power loss occurs in the flow.
- Increase the number and fidelity of the engineering design rules bounding the design space. This could be done by:
  - Studying the aerodynamic performance of conical PFC designs in off-design conditions such as take-off, side-slip angle or high angle of attack. This could lead to various shape constraints (think of intake lip curvature, nacelle inclination angle, fuselage curvature)
  - Linking another engineering discipline to the engineering design application. A first addition could be a structural analysis or weight estimation tool. That could show limits to the nacelle thickness ratio, or show an structural weight improvement for a shorter fuselage.

Regarding parameterization of the propulsive fuselage concept, the following is recommended:

- The maximum fuselage cone angle and its axial location is a valuable parameter to give more control over the fuselage shape. Considering the aerodynamic influence of the fuselage cone, and the potential of shortening it without decreasing its volume, controlling these parameters could lead to significant performance gains.
- The nozzle area is meaningful parameter to control, as it is very indicative of the fan mass flow. If the nozzle area A_{nozzle} and $\frac{dA_{nozzle}}{dx}$ are specified for a given nacelle shape, this makes the outlet and plug shape dependent parameters.
- For conical designs, it is recommended to correct the area of the fan inlet face A_{in} for the angle between it and the incoming (conical) flow direction. That way, the effective duct area reduction at conical inflow is corrected for. This allows a more focused study into the effect that mass flow has on the efficiency of the design.

Regarding the shaping of the propulsive fuselage concept, it is recommended to further increase the conical angle of the tangent of the fuselage contour at the fan inlet face ($\Theta_{in,low}$). This increases cone volume and reduces the cone curvature as long as there is an inflection point in the contour of the fuselage cone. It is believed the highlight area is excessively increased for the most conical designs in this study and this diffuses the flow too much. An increased $\Theta_{in,low}$ could reduce this area back to a more modest highlight area and cause less diffusion before the highlight plane.

Bibliography

[1] EUROCONTROL. *European Aviation in 2040 - Challenges of Growth*. Tech. rep. EUROCONTROL, 2018. url: https://www.eurocontrol.int/sites/default/files/content/documents/official-documents/reports/challenges-of-growth-2018.pdf.

[2] Eurocontrol Statfor. *Forecast Update 2021-2027 European Flight Movements and Service Units Three Scenarios for Recovery from COVID-19*. Tech. rep. EUROCONTROL, Oct. 2021. url: https://www.eurocontrol.int/sites/default/files/2021-10/eurocontrol-7-year-forecast-2021-2027.pdf.

[3] R. S. Nerem et al. "Climate-change–driven accelerated sea-level rise detected in the altimeter era". In: *Proceedings of the National Academy of Sciences* 115.9 (Feb. 2018), pp. 2022–2025. issn: 0027-8424. doi: 10.1073/PNAS.1717312115. url: https://www.pnas.org/content/115/9/2022%20https://www.pnas.org/content/115/9/2022.abstract.

[4] Long Cao, Ken Caldeira, and Atul K. Jain. "Effects of carbon dioxide and climate change on ocean acidification and carbonate mineral saturation". In: *Geophysical Research Letters* 34.5 (Mar. 2007). issn: 1944-8007. doi: 10.1029/2006GL028605. url: https://onlinelibrary.wiley.com/doi/full/10.1029/2006GL028605%20https://onlinelibrary.wiley.com/doi/abs/10.1029/2006GL028605%20https://agupubs.onlinelibrary.wiley.com/doi/10.1029/2006GL028605.

[5] U.S. Global Change Research Program. "Climate Science Special Report". In: *U.S. Global Change Research Program* 1 (2018). Ed. by D.J. Wuebbles et al., pp. 1–470. issn: 0736-6825. doi: 10.7930/J0J964J6. url: https://science2017.globalchange.gov/.

[6] Climate Action Network and International Coalition for Sustainable Aviation. *Contribution of the Global Aviation Sector to Achieving Paris Agreement Climate Objectives*. Tech. rep. Climate Action Network (CAN) and International Coalition for Sustainable Aviation (ICSA), Apr. 2018. url: https://www.theicct.org/aviation..

[7] Mathias Basner et al. "Aviation Noise Impacts: State of the Science". In: *Noise & Health* 19.87 (Mar. 2017), p. 41. issn: 19984030. doi: 10.4103/NAH.NAH{_}104{_}16. url: /pmc/articles/PMC5437751/%20/pmc/articles/PMC5437751/?report=abstract%20https://www-ncbi-nlm-nih-gov.tudelft.idm.oclc.org/pmc/articles/PMC5437751/.

[8] European Commission. *Flightpath 2050, Europe's vision for aviation*. Tech. rep. Luxembourg: European Commission, June 2011, p. 15.

[9] Elisabeth Van der Sman et al. *Destination 2050 - A route to net zero European aviation*. Tech. rep. Amsterdam, NL: NLR, SEO, Feb. 2021. url: https://www.ecac-ceac.org/member-states.

[10] Arne Seitz et al. "Proof of Concept Study for Fuselage Boundary Layer Ingesting Propulsion". In: *Aerospace 2021, Vol. 8, Page 16* 8.1 (Jan. 2021), p. 16. issn: 22264310. doi: 10.3390/AEROSPACE8010016. url: https://www.mdpi.com/2226-4310/8/1/16/htm%20https://www.mdpi.com/2226-4310/8/1/16.

[11] Alejandra Uranga et al. "Analysis of the aerodynamic benefit from boundary layer ingestion for transport aircraft". In: *AIAA Journal* 56.11 (2018), pp. 4271–4281. issn: 00011452. doi: 10.2514/1.J056781.

[12] Valveless Pumps and Václav R Tesaˇtesaˇ. “Viscous Dissipation”. In: *Encyclopedia of Microfluidics and Nanofluidics* (Aug. 2008), pp. 2155–2164. doi: 10.1007/978-0-387-48998-8{_}1669. url: https://link.springer.com/referenceworkentry/10.1007/978-0-387-48998-8_1669.

[13] Hans-Jörg Steiner et al. “Multi-Disciplinary Design and Feasibility Study of Distributed Propulsion Systems”. In: *28 TH INTERNATIONAL CONGRESS OF THE AERONAUTICAL SCIENCES*. ICAS, 2012.

[14] Biagio Della Corte et al. “Power Balance Analysis Experiments on an Axisymmetric Fuselage with an Integrated Boundary-Layer-Ingesting Fan”. In: *AIAA Journal* (Oct. 2021), pp. 1–14. issn: 0001-1452. doi: 10.2514/1.J060570.

[15] Dimitra Eirini Diamantidou, Md Lokman Hosain, and Konstantinos G. Kyprianidis. “Recent Advances in Boundary Layer Ingestion Technology of Evolving Powertrain Systems”. In: *Sustainability* 14.3 (Feb. 2022), p. 1731. issn: 20711050. doi: 10.3390/SU14031731.

[16] Anil Yildirim et al. “Performance analysis of optimized starc-abl designs across the entire mission profile”. In: *AIAA Scitech 2021 Forum* (2021), pp. 1–17. doi: 10.2514/6.2021-0891. url: https://arc.aiaa.org/doi/abs/10.2514/6.2021-0891.

[17] A. L. Habermann et al. “Multidimensional parametric study of a propulsive fuselage concept using openfoam”. In: *AIAA AVIATION 2020 FORUM*. Vol. 1 PartF. American Institute of Aeronautics and Astronautics Inc, AIAA, 2020, pp. 1–18. isbn: 9781624105982. doi: 10.2514/6.2020-2754. url: https://arc.aiaa.org/doi/abs/10.2514/6.2020-2754.

[18] Gaetan K.W. Kenway and Cetin Kiris. “Aerodynamic shape optimization of the STARC-ABL concept for minimal inlet distortion”. In: *AIAA/ASCE/AHS/ASC Structures, Structural Dynamics, and Materials Conference, 2018* 210049 (2018). doi: 10.2514/6.2018-1912. url: https://arc.aiaa.org/doi/abs/10.2514/6.2018-1912.

[19] Anaïs Luisa Habermann, Anubhav Gokhale, and Mirko Hornung. “Numerical investigation of the effects of fuselage upsweep in a propulsive fuselage concept”. In: *CEAS Aeronautical Journal* 12.1 (Jan. 2021), pp. 173–189. issn: 18695590. doi: 10.1007/S13272-020-00487-2.

[20] Martijn Van Sluis and Biagio Dellacorte. *CENTRELINE D3.03-Final PFC Aircraft Aerodynamic Design and Performance Deliverable submission date D3.03-FINAL PFC AIRCRAFT AERODYNAMIC DESIGN AND PERFORMANCE*. Tech. rep. 2020. url: www.centreline.eu.

[21] Jason Welstead. *Overview of the NASA STARC-ABL (Rev. B) Advanced Concept*. Mar. 2017. url: https://ntrs.nasa.gov/citations/20170005612.

[22] Jesús Matesanz-García et al. “An Automated Approach for the Aerodynamic Design of Close-Coupled Propulsion/Airframe Configurations”. In: *Proceedings of Aerospace Europe Conference 2020* (Feb. 2020). url: https://dspace.lib.cranfield.ac.uk/bitstream/handle/1826/15307/close-coupled_propulsion-airframe_configurations-2020.pdf?sequence=4&isAllowed=y.

[23] Mark Drela and T. J. Kohler. “Power balance in aerodynamic flows”. In: *AIAA Journal* 47.7 (July 2009), pp. 1761–1771. issn: 00011452. doi: 10.2514/1.42409.

[24] Lex Lv. “Theoretical and Experimental Investigation of Boundary Layer Ingestion for Aircraft Application”. PhD thesis. 2019. doi: 10.4233/uuid:6d8bd168-e057-4ee9-854c-32c84015e4c4. url: https://doi.org/10.4233/uuid:6d8bd168-e057-4ee9-854c-32c84015e4c4.

[25] Frank M. White, Chiu-On Ng, and Saroj Saimek. *Fluid Mechanics*. 7th. New York, USA: McGraw-Hill Education, 2011.

[26] Brenda M. Kulfan and John E. Bussoletti. “”Fundamental” parametric geometry representations for aircraft component shapes”. In: *Collection of Technical Papers - 11th AIAA/ISSMO Multidisciplinary Analysis and Optimization Conference* 1 (2006), pp. 547–591. doi: 10.2514/6.2006-6948. url: https://arc.aiaa.org/doi/abs/10.2514/6.2006-6948.

[27] Brenda M. Kulfan. “Universal Parametric Geometry Representation Method”. In: *Journal of Aircraft* 45.1 (Jan. 2008), pp. 142–158. issn: 15333868. doi: 10.2514/1.29958. url: https://arc.aiaa.org/doi/abs/10.2514/1.29958.

[28] Robert Christie et al. “The use of hybrid intuitive class shape transformation curves in aerodynamic design”. In: *Aerospace Science and Technology* 95 (Dec. 2019), p. 105473. issn: 1270-9638. doi: 10.1016/J.AST.2019.105473.

[29] M van Sluis, B DellaCorte, and A Gangoli Rao. “Aerodynamic Design Space Exploration of a Fuselage Boundary Layer Ingesting Aircraft”. 2020.

[30] *ISO 2533:1975(en), Standard Atmosphere*. url: https://www.iso.org/obp/ui/#iso:std:iso:2533:ed-1:v1:en.

[31] Hermann Schlichting. *Boundary Layer Theory*. Ed. by Jack P. Holman. 7th. McGraw-Hill Book Company, 1979. url: http://ae.sharif.edu/~viscousflow/Schlichting%20-%20Boundary%20Layer%20Theory.pdf.

[32] Martijn van Sluis, Anais Habermann, and Julian Bijewitz. *D2.03 – Report on Aerodynamic Design Space Exploration*. Tech. rep. CENTRELINE consortium, June 2019.

[33] Andreas Peters et al. “Ultrashort nacelles for low fan pressure ratio propulsors”. In: *Journal of Turbomachinery* 137.2 (Feb. 2015). issn: 15288900. doi: 10.1115/1.4028235.

A
Appendices

A.1. Appendix A: Named expressions

The following list contains the definitions of *named expressions* (in Fluent syntax) that are used to define boundary conditions in Fluent. These definitions are the implementation of equations described in chapter 2. Note that Fluent uses gauge pressures, relative to the reference ambient static pressure.

```
T_0_in : Average(TotalTemperature, ['engine_intake'])
T_0_out : T_0_in * FPR^((gamma-1)/gamma)
h_0_in: MassFlowAve(SpecificTotalEnthalpy,['engine_intake'])
h_0_out: MassFlowAve(SpecificTotalEnthalpy,['engine_outlet'])
P_fan: mass_flow_out * (h_0_out - h_0_in)
mass_flow_in: abs(MassFlow(['engine_intake']))
mass_flow_out: abs(MassFlow(['engine_outlet']))
p_0_in: AreaAve(TotalPressure,['engine_intake'])
p_0_out: (p_0_in + p_amb) * FPR - p_amb
p_s_in: AreaAve(StaticPressure,['engine_intake'])
p_s_out: AreaAve(StaticPressure,['engine_outlet'])
fan_force: mass_flow_in*(MassFlowAve(Velocity.x,['engine_outlet']) -
                         MassFlowAve(Velocity.x, ['engine_intake'])) +
           area_out * p_s_out - area_in * p_s_in

pressure_force: PressureForce(['skin']).x
viscous_force: ViscousForce(['skin']).x
surface_force: pressure_force + viscous_force
net_vehicle_force: fan_force - surface_force
```

A.2. Appendix B: Calculation of target NPF

A top level requirement of the APPU concept is that the BLI fan produces 10% of the aircraft cruise thrust. In cruise, thrust equals drag following from axial force equilibrium.

The drag of APPU's baseline A321 Neo aircraft is assumed to equal the (unknown) drag of the APPU configuration. This simplification is made because the installed BLI propulsor increases drag, but as the under-wing engines can be sized smaller, the net drag addition is hard to quantify, making the drag estimation of a APPU configuration less credible. The aircraft weight mid-cruise is assumed to be the average mission weight. With the A321 Neo take-off weight (93.5 tons) and landing weight (77.3 tons), the mid-cruise weight is then approximated as: $W_{mid,cruise} = 8.37 \times 10^5 N$.

The TU Delft in house mission calculator tool *Initiator* estimates the A321 Neo's cruise lift-to-drag ratio $\frac{L}{D}$ to be 16.3. Using this ratio, the cruise drag is estimated to be $D_{mid,cruise} = 51.3 \times 10^3 N$. The thrust demanded from the BLI propulsor (10% of total) is therefore $D_{mid,cruise} = 5.13 \times 10^3 N$.

As the use of thrust and drag is avoided in this research, it is interpreted that the installation of the BLI propulsor should have a net propulsive force of at least $NPF_{mid,cruise} = 5.13 \times 10^3 N$. This value is used as the target NPF.